

## **A. Supplementary Methodology Details**

This appendix is an addendum to Chapter 3 and provides supplementary information regarding data acquisition, methodologies employed, their rationale, and scientific basis.

### **A.1 Field Data Collection**

Structural measurements were recorded using either a Brunton (Eclipse and GeoTransit), Freiberg, or Suunto compass clinometer. Where possible, locations of structural measurements and sample collection sites were recorded using a handheld Garmin GPS receiver, however, due to the height of the pit walls the accuracy of GPS data was sporadically compromised. Where the GPS unit reported an accuracy of greater than  $\pm 3$  metres sample/measurement locations were determined by triangulation from control point stakes situated at various points within the open pits. The locations were marked on paper maps and subsequently converted into UTM coordinates using Manifold<sup>TM</sup> software.

The locations of underground measurements were recorded by measuring the distance and direction from marked survey points on drift walls. Steel bolts and mesh were present in potentially unstable areas of the underground workings. These can deflect the magnetic compass needle and result in false readings. To reduce the potential for compromised accuracy of collected data, care was taken to avoid recording structural measurements

proximal to bolts or mesh. Due to the presence of mine traffic and safety concerns, underground mapping was generally limited to time periods between shift changes. This allowed for 2 hours of mapping each evening and one full day every two weeks.

UTM coordinates, structural measurements, photograph details, and observations on structure, lithology, and alteration were recorded in a notebook, and transferred on a nightly basis to a Microsoft Access database, and to a Microsoft Excel spreadsheet for subsequent statistical analysis and use in GIS software (Appendix B, C, and D). Planar structural elements were recorded as dip/dip direction (subsequently converted to dip/strike in Microsoft Excel<sup>TM</sup>). Linear structural elements were recorded as plunge/azimuth, or where necessary trend/rake.

#### **A.1.1 Statistical Analysis of Field Data**

Measurements were entered into the Pangaea Scientific's Spheristat<sup>TM</sup> stereographic projection software to assess trends in the data. Equal area lower hemisphere projections, and weighted rose diagrams were generated. Typically, planes were plotted as poles to planes, while lineations orientations were plotted as points. Where there was a large quantity of data, and trends were ambiguous, the data was contoured using a Gaussian distribution model where kurtosis ( $K$ ) = 100. Contour increments are in standard deviations above the mean, whereby an average population density is calculated for  $8.1^\circ$  areas of the lower hemisphere projection. As such, if a given  $8.1^\circ$  area has a population

density above the 75th percentile to the mean, it will fall within the two standard deviations contour. In addition, to analyse stress vectors for a given fault population, fault orientation data and slip vector data was entered into Pangaea Scientific's MyFault™ software or FaultKin™ 8.1 software. Faults within each data set would be assigned a weighting of 1 to 4, based on observable fault width and length, and a confidence value of 1 to 4, based on the confidence placed in the slip vector orientation. If a fault displayed a clear offset or deflection of marker horizons or structures, or had consistently well developed and uniformly oriented slickensides/slickenlines and associated steps the fault was assigned a confidence value of 4, while a fault with weakly developed slickensides/slickenlines would be assigned a confidence value of 1. For the shortening and extension direction calculations, where a fault surface showed multiple, contradictory slip vector orientations, the fault would be considered to have experienced multiple discrete slip events and as such would be entered into the calculation as two discrete faults, with confidence values applied to each set of slip vectors.

## **A.2 Additional Available Data**

Below is a complete list of data supplied to the author throughout the course of the study:

- Borehole database current to May 2010 containing data for 18,611 boreholes;
  - Data for 629 boreholes drilled by Alexco between 2006 and May 2010;
    - 283 overburden boreholes (equal to or less than 7.5 m depth); drilled into the proposed tailings pond;

- 346 diamond drill boreholes (maximum depth 642.82 m) covering at least 14 prospects or deposits within the district;
  - Data for 17,982 historic (pre-2006) boreholes; including
    - 14,698 overburden boreholes (maximum depth 100.58 m);
    - 2,141 diamond drill boreholes (maximum depth 494.39 m);
    - 1,143 boreholes of unknown origin;
  - Due to the long history of mining and exploration within the Keno Hill mining district the integrity of data from the historic boreholes is commonly questionable. Conflicting, poorly recorded, or lost data is common. As such, much of the interpretation in this study is reliant on data acquired by Alexco between 2006 and 2010.
- Remote sensing data;
  - Airborne magnetic data and accompanying report acquired by Alexco in 2006 (McPhar, 2006). The data was received as Surfer™ gridded data and was processed by the author prior to use;
    - Data has 1,808 kilometers of flight lines at 360° with a 200-metre line spacing flight lines, and 208 kilometres or tie lines with a 2,000-metre line spacing at 090°. Data is gridded with 60 metre cells. Magnetic data filter derivatives supplied included:
      - Reduction to pole (RTP); and
      - First vertical derivative (1VD).
  - SkyTEM airborne magnetic, electromagnetic, resistivity, and elevation data acquired by Monster Mining Corporation in 2011, and supplied to the

author by Metallic Minerals Corporation in 2017. Data was supplied as four individual Geosoft™ grids for the Beauvette, DFCH, Homestake, and Mount McFaul claims;

- Data has 100-metre line spacing flight lines, gridded with 30 metre cells: Magnetic data filter derivatives supplied included:
  - First vertical derivative (1VD);
  - Total magnetic intensity (TMI);
  - Residual magnetic field (RMF); and
  - Additional magnetic data were provided as processed GeoTiff files with the 1VD, 2VD, AS, THG, and TMI products supplied.
- Regional airborne magnetic and gravity geophysical data obtained from the YGS covering the Yukon, British Columbia, and Alaska;
  - Composite residual total field (RTF) and 1VD airborne magnetic data (250 to 800 metre line spacing; Oneschuk et al., 2019);
  - Canada-wide RTF and 1VD airborne magnetic data (250 to 800 metre line spacing; Miles and Oneschuk, 2016);
  - Canada wide gravity anomaly data (data spacing ranges from less than one kilometre to greater than 20 kilometres, with an average of 15 kilometres; Jobin et al., 2017).
- High resolution aerial photographs covering the Keno Hill district acquired by Alexco;
  - 5 metre resolution topographic data acquired by Alexco and derived from aerial photography survey;

- Orthorectified LandsAT 7 data acquired from [www.geobase.ca](http://www.geobase.ca); the band combination 7-4-1.
- 2D and 3D deposit- to regional-scale maps, interpretations, and reports;
  - Historic level plans and cross-sections for the Bellekeno, Bermingham, Elsa, Hector-Calumet, Husky, Keno 700, Lucky Queen, Onek, Shamrock, Silver King, and Sime (Galkeno) deposits;
  - .dxf wireframes for faults, veins, and lithological contacts interpreted by Alexco;
  - .dxf infrastructure wireframes for the Bellekeno, Black Cap, Dixie, Elsa, Flame and Moth, Galkeno, Hector-Calumet, Husky, Keno 700, Lucky Queen, No Cash, Onek, Ruby-Bermingham, Sadie Ladue, Shamrock, Silver King, and Townsite underground workings;
  - Mapinfo™ table files for district-scale mapping of the Keno Hill area by Alexco;
  - 1:250,000 scale maps (as shapefiles) covering the bedrock geology, surficial geology, geochronology, stream geochemistry, and mineral occurrences in the Yukon; supplied by the YGS; and
  - Numerous assessment reports and internal reports supplied to the author by Alexco.

### **A.3 Remote Sensing Data Acquisition**

The following section briefly describes the fundamental techniques for acquiring the remote sensing data analysed in this thesis.

#### **A.3.1 Helicopter Magnetic Data Survey Acquisition**

The following section describes the acquisition of the helicopter magnetic survey, more detail on the survey parameters can be reviewed in McPhar's (2006) report. It should be noted that the details supplied below refer only to Alexco's acquisition of airborne magnetic data in 2006, no details were available to the author describing the acquisition of the data supplied by Metallic Minerals.

A high-resolution magnetic and time domain electromagnetic (THEM – Time-domain Helicopter ElectroMagnetic) survey was flown over a 361.6 kilometre square area in the

Keno Hill region (Figure A.1;

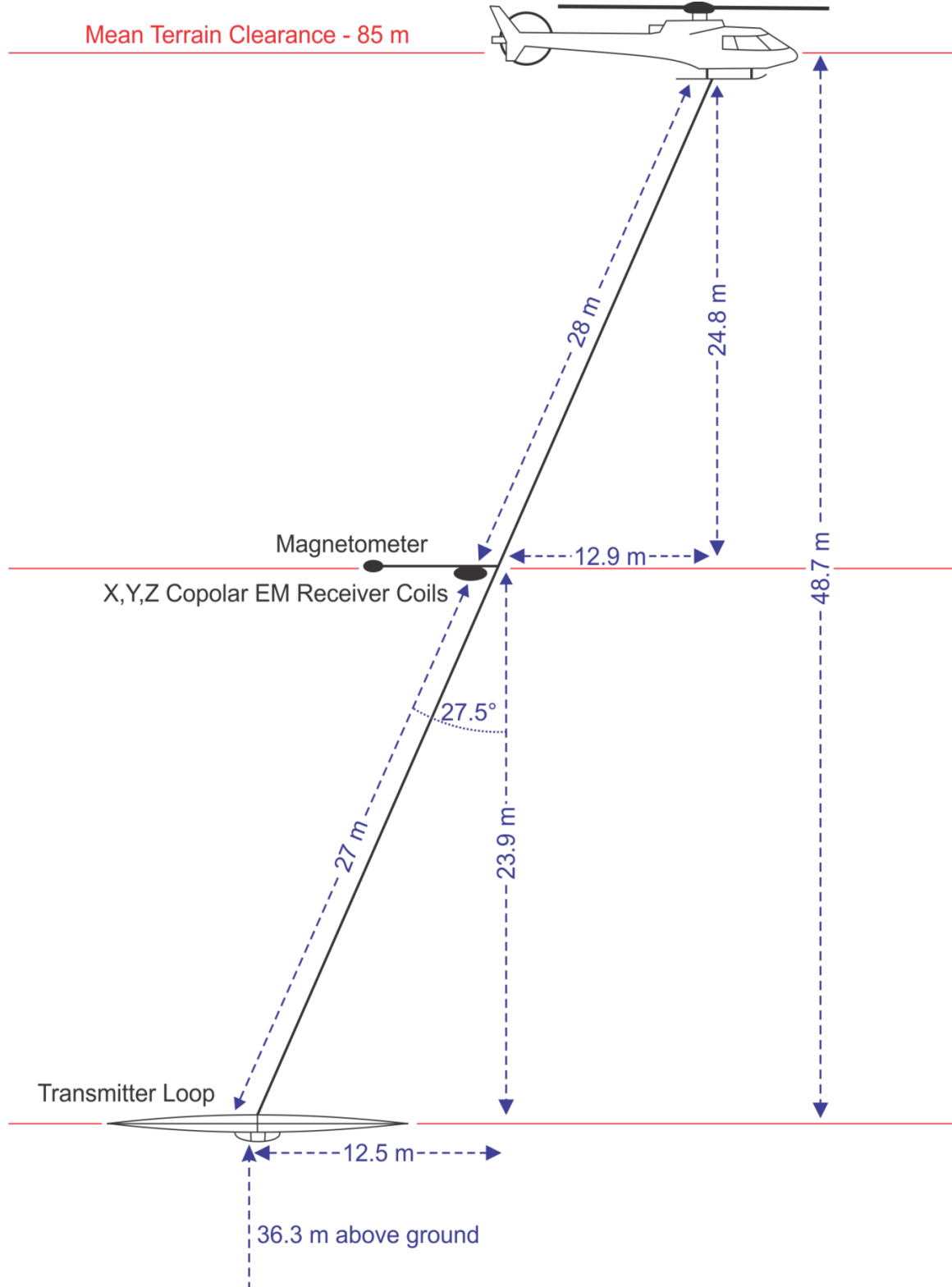
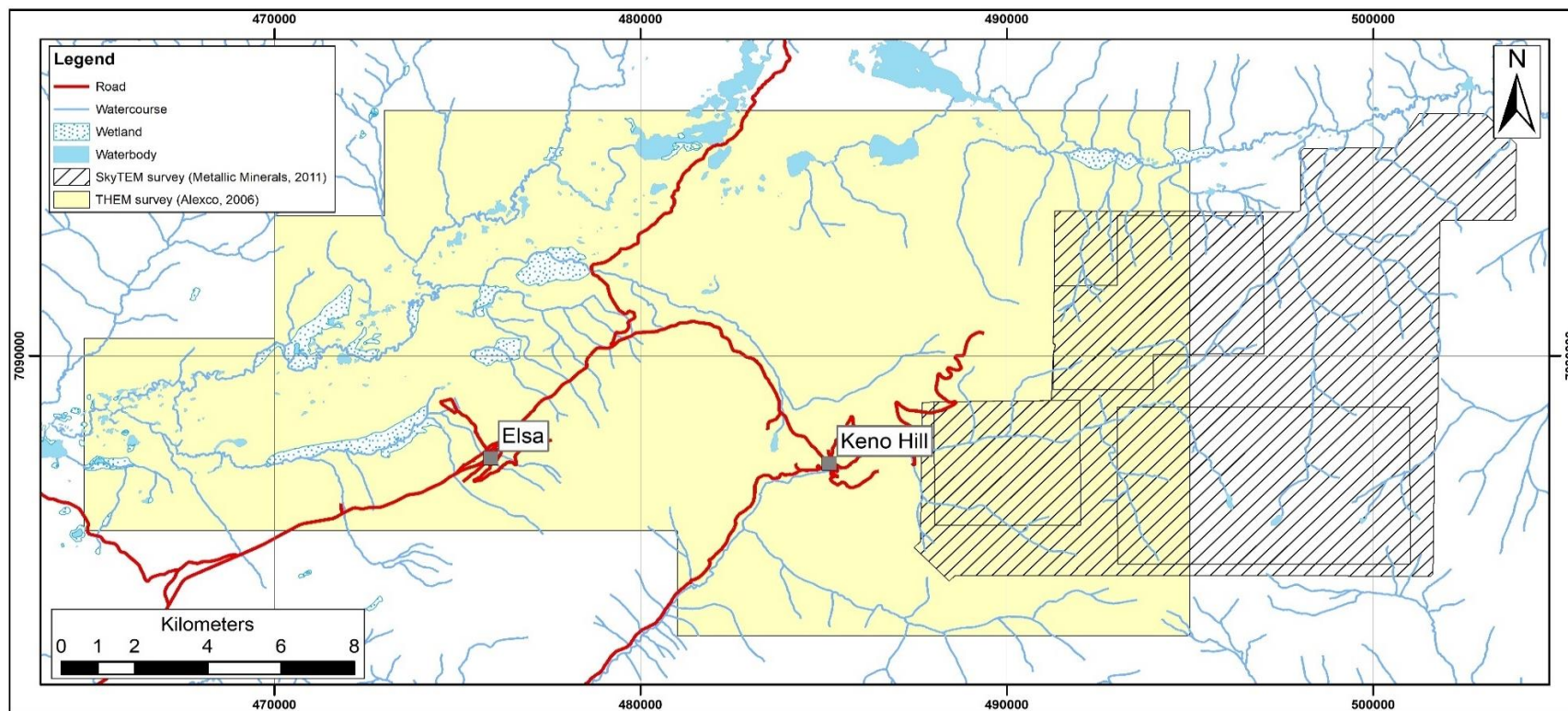




Figure A.2: Helicopter magnetic and THEM survey configuration (modified from McPhar, 2006).

Table A.1). The THEM geophysical system was mounted on Eurocopter AS-350B2 helicopter, and acquisition involved the use of precision real-time differential GPS positioning and a high sensitivity magnetometer system incorporated into the THEM system towed beneath the helicopter (Figure A.2). The survey was flown along a north-south line ( $360^{\circ}$ ) at spacing of 200 metres and tie lines flown in east-west direction ( $90^{\circ}$ ) at spacing of 2,000 metres (McPhar, 2006).



**Figure A.1: Map showing limits of the Alexco's 2006 helicopter magnetic and THEM survey and Metallic Mineral's 2011 SkyTEM survey.**

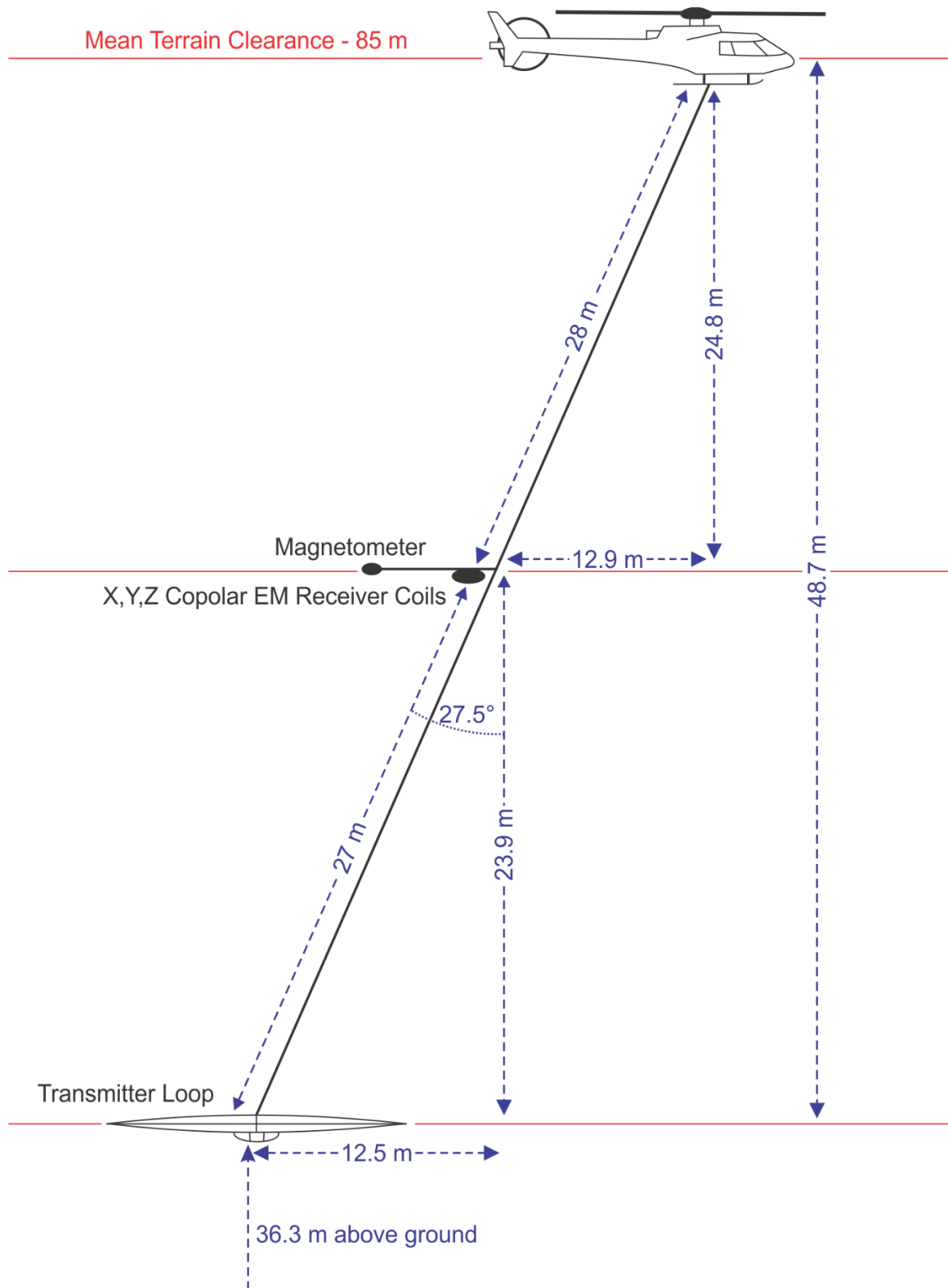


Figure A.2: Helicopter magnetic and THEM survey configuration (modified from McPhar, 2006).

**Table A.1: Boundary co-ordinates for helicopter magnetic survey.**

UTM Easting	UTM Northing
495000	7082000
481000	7082000
481000	7085000
464800	7085000
464800	7090500
470000	7090500
470000	7094000
473000	7094000
473000	7097000
495000	7097000

The magnetic sensor utilized for the survey was a Geometrics G-822A optically pumped cesium vapour magnetic field sensor, mounted on a boom. The reported sensitivity of the magnetic sensor is 0.0005 nanoTesla (nT) at a sampling rate of 20 times per second (McPhar, 2006).

Processing of the acquired data was completed by McPhar Geosurveys Ltd. and involved the application of traditional corrections to compensate for diurnal variation, lag, heading effects and levelling prior to gridding. This included:

- Correction for diurnal variation using the digitally recorded ground base station magnetic values;
- Adjustment of the data for the time lag between the GPS position and the position of the magnetic sensor;
- Network adjustment using the flight line and tie line information to level the survey data set; and

- Subtraction of International Geomagnetic Reference Field (IGRF) calculated for model year 2005.

The corrected data was used to generate a Total Magnetic Intensity (TMI) grid. Corrected magnetic line data were interpolated between survey lines using a random point minimum curvature gridding algorithm to yield x-y grid values for a standard grid cell size of 1/3rd of the nominal flight line spacing (a 60 metre grid cell) (McPhar, 2006).

A series of spatial filtering techniques were applied to the TMI data using the Oasis Montaj Magmap module that yielded colour/contour images of the following:

- Reduction to the pole (RTP);
- Calculation of the first vertical derivative (1VD);
- Calculation of the second vertical derivative (2VD);
- Calculation of the horizontal gradient; and
- Calculation of the analytic signal (AS)

The true magnetic anomaly position over the source may be shifted by the magnetic inclination and declination of the magnetic field at a given location on the Earth. To compensate for the shift, the magnetic data were recomputed so that magnetic anomalies appear as if located at the north magnetic pole. The result of this operation is that in theory, the magnetic anomaly is located directly above the source. The computation is referred to as "reduction-to-the-pole" (RTP) and is computed using a FFT (Fast Fourier Transform) operation. The RTP not only shifts the anomalies to their correct position with respect to the causative magnetic bodies, but assists in the direct correlation and

comparison of magnetic anomalies, trends, structural axis, and discontinuities with mapped geologic surface expression. The RTP was calculated using the following parameters for the survey area:

- Geomagnetic Inclination:  $78.5^{\circ}$  N
- Geomagnetic Declination:  $+25.6^{\circ}$

The vertical derivative indicates the rate of change of the magnetic field with height. The first vertical derivative (1VD) has the effect of sharpening anomalies and therefore allowing for improved spatial location of source axes and contacts. The 1VD was calculated from the grid of RTP of the TMI after IGRF correction.

The data sets supplied by Alexco and Metallic Minerals are of varying vintage, and have varying flight line directions, flight line spacing, and acquisition height. As such prior to the district-scale interpretation the various datasets were compiled and levelled by Ronacher-McKenzie Geoscience, on behalf of the author.

### **A.3.2 Orthophotographic and Topographic Data Acquisition**

The colour aerial photographic (orthophotographic) data were acquired by Alexco from Aero Geomatics in July 2006. The aerial photography comprised 376 photographs and covered a 480 kilometre square area (O'Connor et al., 2007). Associated survey control was performed by registered surveyors Aucoin Surveys, Ltd. The photography was

completed in the fall of 2006 after all snow cover had disappeared and a succession of clear days allowed for optimum conditions. A photographic mapping camera with a focal length of 153 millimeter (6 inches) was used and negatives were scanned to produce digital images. Further work utilizing photogrammetry computer software resulted in orthophotographs and a digital stereo compilation, which was used to generate surface topographic contour maps at a scale of 1:10,000 (O'Connor et al., 2007). The DEM was derived from the topographic contour maps, where the scale of 1:10,000 is approximately equivalent to a cell size of 5 metres per pixel. The final delivered data covered an area of 220 kilometres squared (O'Connor et al., 2007).

#### **A.4 Post-Processing and Preparation of Remote Sensing Data**

##### **A.4.1 Magnetic Data**

The district- and regional-scale magnetic datasets were supplied to the author as levelled Geosoft<sup>TM</sup> grid files. The data were imported into Geosoft Oasis Montaj<sup>TM</sup> viewer and converted to binary (DOS) grid files. The data were subsequently imported into ERMapper<sup>TM</sup> for processing. Prior to the interpretation an intensity layer was added to the file, and the colour profile and sunshade direction was manipulated to enhance the structures present. Three sunshade directions were used to highlight structures in different orientations; these directions were 000°, 045°, and 315°. Colour density and shaded relief images were produced (Figure A.3). The data were exported from ERMapper<sup>TM</sup> as

compressed images (.ecw) files for use in ArcGIS™ software. The district-scale interpretation was completed at a scale of 1:25,000, and regional-scale interpretation was completed at a scale of 1:250,000.

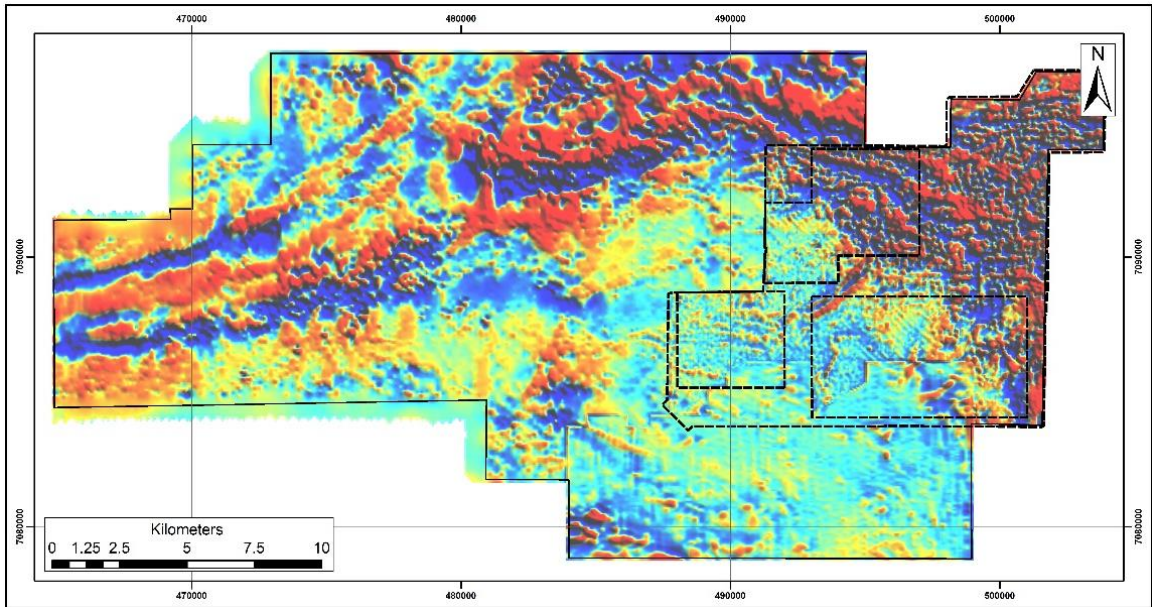


**Figure A.3: Levelled 1VD data used for 2D interpretation of airborne magnetic data. Dashed lines indicate data supplied by Metallic Minerals.**

#### **A.4.2 DEM Data**

The DEM data was supplied to the author as a Surfer™ grid file. The data were converted to binary (DOS) grid files using Geosoft Viewer™ software. An intensity layer was added to the file, and the colour profile and sun shade direction was manipulated to produce a shaded relief image in ER Mapper™ (Figure A.4). The image was subsequently exported as a compressed .ecw file for use in ArcGIS™.



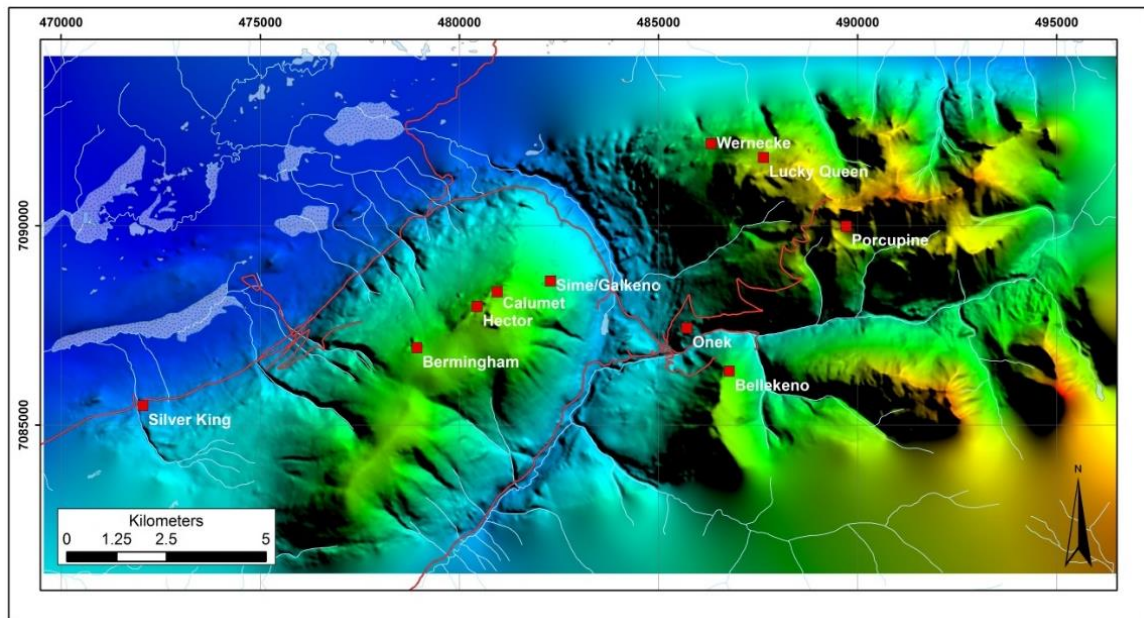


**Figure A.4: Shaded-relief image of DEM data.**

### **A.4.3 Orthophotographic Data**

The orthophotographic data was supplied to the author as eight georeferenced .ecw files each containing natural colour images for a portion of the study area. Each image covered an area of approximately 21 kilometres squared. The eight supplied images were imported and mosaiced in ERMapper™, and exported as a single georeferenced .jpeg file (.jgw) for use in Arc GIS™ (Figure A.5). No additional filters or processing techniques were applied to the images.

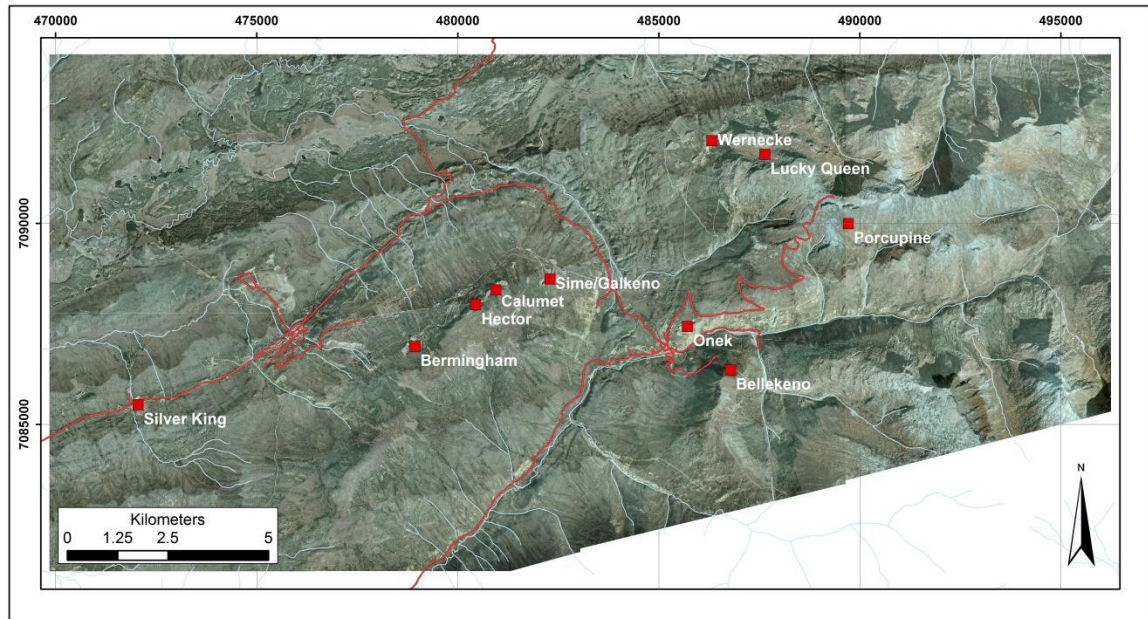


**Figure A.5: Mosaic of orthophotographic data.**

## **A.5 Two Dimensional (2D) Structural Lineament Interpretation**

The following section summarises the key methodologies and parameters employed in the interpretation of the district-scale and regional-scale airborne magnetic datasets. The interpretations were completed done both within the context of known structural models evinced in the field by structural observations (e.g., thrust duplex systems), and through structural section balancing, as well as incorporating cross-cutting relationships and the known age relationships in the area of study. This produces a holistic interpretation and a geometrically robust interpretation.

It is important that an understanding of data derivation is incorporated in this process; the magnetic source for the bedrock lineament interpretation is a swath of magnetic response through the earth's crust and is not representative of the bedrock response at surface. Therefore, lineaments observed in the magnetic data may appear to shift in the surficial (orthophotographic and DEM) datasets depending on their dip. In addition, available district-scale magnetic datasets had varying resolutions, thus, regardless of data resolution, the district-scale interpretation for all datasets was completed at a scale of 1:25,000 to ensure no scale bias was introduced. The regional interpretation was completed on a single, magnetic compilation dataset. The compilation includes relatively high-resolution airborne surveys (250 to 500 metre line spacing); however, for the area of interest the line spacing for the survey is relatively coarse (800 m). As such the regional interpretation was completed at a scale of 1:250,000.

Each identified lineament was classified in an attribute table in ArcGIS™. The description of the attribute fields used is included in Table A.2. Metadata for the interpretation is provided in Appendix D within a series of ArcGIS™ map packages and provides information on fault order, fault length, fault strike, and interpreted fault age.

The interpretation followed a process that is outlined below:

**Table A.2: Attribute table fields populated for the lineament interpretation**

Attribute	Description
Rel_age	Interpretation of relative age of feature, in accordance with regional structural history
Flt_Order	Value describing the authors assessment of fault scale (1-major, 2-intermediate, or 3-minor)
Length	Length of feature segment expressed in metres.
Azimuth	Lineament orientation expressed as degree rotation between 0 and 359 degrees. Azimuth is measured at the midpoint of the line.

## **1. Interpretation of Magnetic Data:**

- a. **Formline Mapping:** Tectono-stratigraphic form lines were drawn using the 1VD data. Form lines trace the geometry of stratigraphy and tectonic fabrics within volcanic and metasedimentary rocks or the internal fabric (foliation) within intrusive rocks. Discontinuities between form lines, particularly stratigraphic form lines (e.g., intersecting form lines) highlight structures (faults, folds), unconformities, or intrusive contacts.
- b. **Fault and Shear Zone Mapping:** A structural base layer was drawn using the 1VD data representing all faults regardless of interpreted age, style (e.g., brittle versus ductile), or kinematics. Evidence for interpreted fractures can be derived from several sources in the magnetic data, including discontinuities between form lines, offset of magnetic units, or the presence of linear magnetic lows or high. The first vertical derivative magnetic data was used with the tilt angle grid used to augment the interpretation.

- c. **Assessment of Age Relationships:** Relative age and cross-cutting relationships were defined between different families of structures. This incorporated a working knowledge of the structural history of the project area. Mutually cross-cutting faults and shear zones are not naturally occurring; therefore this part of the methodology requires that no-two lineaments be mutually cross-cutting, and thus interpreted older lineaments are typically offset by or truncated against younger lineaments. At this stage the potential for fault reactivation is taken into consideration, whereby interpreted older structures may have been reactivated during later deformation phases and thus appear to offset faults of a younger interpreted age.
  - d. **Estimation of Structure Scale:** An estimation of fault/shear zone order (i.e., 1st, 2nd, 3rd order) was attributed. This process identifies the locations of major structures versus subsidiary structures. At this stage structure length is also calculated. Lineament lengths were calculated using a simple geometrical calculation of the total length of the polyline in ArcGIS™.
2. **Statistical Analysis of Lineament Trends:** An analysis of lineament trends is an essential part of the structural lineament interpretation. It allows the

interpreter to identify different sets of structures and to relate those sets to the known structural history of the area. Lineament orientations were assessed for the Keno Hill area to determine the dominant lineament trends, and potential conjugate sets. Lineament orientations (strike) were calculated using ET EasyCalculate 10, an add-in extension to ArcGIS™. This add-in provides a function (polyline\_GetAzimuth.cal) that calculates the azimuth of each polyline at a user-specified point and populates an assigned attribute field. The author used the mid-point of each interpreted lineament to calculate the azimuth.

Rose diagrams (circular or semi-circular histograms) that depict orientation (azimuthal) data and frequency for each dataset were created. The histogram peaks show the frequency of occurrence of lineament orientations within each bin. Rose diagrams were produced in Spheristat™, with frequencies divided into 5° bins. Lineament lengths were used as a weight factor for computing rose diagrams.

3. **Calculation of Lineament Density:** Lineament density calculations provide insight into areas of increased structural complexity that may be associated with areas of increased fluid flow and elevated mineralisation. The lineament density analysis was conducted using the ArcGIS™ Analysis and Spatial Analyst toolsets, and included creating lineament density plots for the airborne magnetic data sets.

Lineament line density of all interpreted lineaments in the Keno Hill area was determined by examining the statistical density of individual lineaments using ArcGIS<sup>TM</sup> Spatial Analyst. A grid cell size of 25 metres and a search radius of 1,000 metres were used for this analysis. The spatial analysis used a circular search radius examining the lengths of polylines intersected within the circular search radius around each grid cell.

#### **A.6 Three-Dimensional (3D) Analysis**

Three-dimensional (3D) analysis of subsurface data, including borehole data, surface and sub-surface *in situ* measurements, and magnetic data was completed for the Keno Hill area to determine and visualise the 3D structural architecture and its relationship to Ag-Pb-Zn mineralisation (Appendix D). The analysis was completed in Leapfrog Geo<sup>TM</sup> 3.0 software. Leapfrog Geo<sup>TM</sup> has several functions that allow rapid modelling and analysis of subsurface datasets. A brief synopsis of the techniques used during the 3D analysis is presented below.

### A.6.1 Data Processing

The database was supplied to the author in the NAD83 UTM Zone 8N datum. The database contained data for 18,611 boreholes from numerous drilling phases dating from August 1930 to August 2009. The database includes surficial and underground diamond drill, reverse circulation (RC), overburden, and sonic drilling data.

Collar, survey, assay, lithology, structure, alteration, mineralisation, and geotechnical tables were entered into Leapfrog Geo™ using the *import drillholes* function. When importing the collar file columns including the borehole identifier, easting, northing, elevation and maximum depth were imported, however additional empty columns were added to the table for later use when querying or subsetting data by location or deposit. Due to the very large size of the database and the old age of some of the boreholes, numerous errors were encountered in all tables. The errors included, but were not limited to missing survey data, mismatches between the stated maximum depth and the measured maximum depth drill holes and overlapping intervals in the assay or lithology tables. As far as possible and without compromising the integrity of the dataset, the errors were corrected using the *fix errors* function for each borehole individually. Once errors had been corrected to an acceptable level, the dataset tables were exported to Excel™, saved as individual .csv files and reimported into Leapfrog Geo™. This process means that if, for any reason, the Leapfrog Geo™ project needs to be rebuilt, the error corrections do not have to be repeated.



Subsequent to importing the drill hole data a topography file was added (described in Appendix A.2 and A.3.2). After importing the topography layer, it was evident that some of the collar locations were incorrect. Collars that were in error projected above or below the topography and distal to any underground workings. In addition, some boreholes had inverted survey data, whereby the drill string projected above topography. The errors were largely encountered in historic boreholes, presumably due to less accurate spatial referencing techniques than used today. Borehole collars that were deemed to be in error were manually selected and a subset of these collars was created in one of the empty columns imported with the collar file. The subsets of the collars in error and the correct collars were exported to individual Excel<sup>TM</sup> files, and saved as individual .csv files. The collars-in-error file was imported into Leapfrog Geo<sup>TM</sup> and the *move collars to topography* function was applied to reassign the collar elevations. No adjustments were made of the northing or easting coordinates. This collar file was exported to Excel<sup>TM</sup>, merged with the correct collar file, and reimported into Leapfrog Geo<sup>TM</sup>.

The orthophotographic data, numerous regional to district scale maps, open pit maps created by the author following the site visits, and the geophysical data were imported as .jpeg files into Leapfrog Geo<sup>TM</sup> and georeferenced using the *import map* function. This function allows for maps and images to be draped onto the topography. Where available, .dxf (Digital eXchange Format) files containing wireframes of the historic workings for the various deposits in the area were imported using the *import mesh* function. In addition, the lineament interpretation derived from the 2D analysis of the geophysical

data was imported into Leapfrog Geo™ as a shapefile (.shp). This was used to guide the location and trend when modelling major faults and shear zones in the 3D model.

The lithology table within the borehole database contains 35 discrete lithological codes describing individual rock types. The large number of lithological codes can be, in part ascribed to sporadic typographical errors by an individual logger (e.g., QTZY instead of QTZT for quartzite); however, much of the variation in the data is attributed to the long exploration and mining history of the district, and variations in logging methodology and individuals logging the core. Large numbers of lithological codes that often describe the same rock type significantly inhibit the ability to accurately define lithological and structural relationships within a model and introduce redundancy into the modelling process. As such, lithological data were simplified by grouping similar lithological codes together using the *add column → group lithologies* function in Leapfrog Geo™. This resulted in 13 grouped lithological units (Table A.3). The grouped lithologies column was duplicated in the lithology table (and renamed GM\_Lith) to allow for subsetting the lithology code.

**Table A.3: Grouped lithologies used in 3D modelling.**

<b>Original Logging Code</b>	<b>Lithology</b>	<b>Grouped Lithology</b>
BED	Unknown	No Data
CAS	Casing	
ND	No Data	
NR	No Recovery	
Blank	No Data	
UNKN	Unknown	
MQTS	Unknown	
MSQT	Unknown	
OVB	Overburden	Overburden
CALCSIL	Calcareous Siltstone	Calcareous Schist
CASLST	Calcareous Siltstone	
CSCH	Calcareous Schist	Chlorite Mica Schist
CHSCH	Chlorite Mica Schist	
SSCH	Sericite Schist	Graphitic Schist
Cb_SLST	Carbonaceous Siltstone	
PHY	Graphitic Phyllite	
G_SLST	Graphitic Siltstone	
SLST	Siltstone	
SCH	Schist	
Q_SLST	Quartz Siltstone	
GSCH	Graphitic Schist	Quartzite
QTZT	Quartzite	
QTZY	Quartzite	
CQTZT	Calcareous Quartzite	
LMST	Limestone	Greenstone
GNST	Greenstone	Monzonite
MONZ	Monzonite	
Q_MONZ	Quartz Monzonite	Quartz Feldspar Porphyry
QFP	Quartz Feldspar Porphyry	
HFPORPH	Feldspar Porphyry	Breccia
Q_BX	Quartz Breccia	Fault
FLT	Fault	
VM	Vein (Massive)	Vein
VN	Vein	
SKARN	Skarn	Skarn

### **A.6.2 3D Modelling Methodology**

3D modelling of Ag grade was completed on each of 10 geographic domains/structural domains; detailed fault and vein modelling was completed for the Galena summit domain (Figure A.6). Leapfrog Geo<sup>TM</sup> contains a function called *Geological Model*; this function allows for the user to define a stratigraphy prior to building the model, and to delineate a fault history. A “geological model” was built for each of the modelled domains, and the GM\_Lith column was used as the base lithology for the stratigraphy. The 3D modelling was an iterative process, thus, while the methodologies used for Ag-grade and structural modelling are outlined individually below, it must be noted that outlined methodologies are not necessarily listed in chronological order, and that modifications to all elements of the models were made throughout the modelling process.

#### **A.6.2.1 Ag, Pb, and Zn Grade Modelling**

Grade modelling was completed for each of the major economic elements present within the Keno Hill District (i.e., Ag, Pb, and Zn). Grade shells were initially produced for the entire Keno Hill district, and subsequently for each domain (Figure A.6). The initial modelling of grade was completed using an isotropic analysis of grade to assess overall mineralised trends in the district, with subsequent modelling iterations refined using structural trends based on geological knowledge of the district. The various methodologies for grade modelling are outlined below.

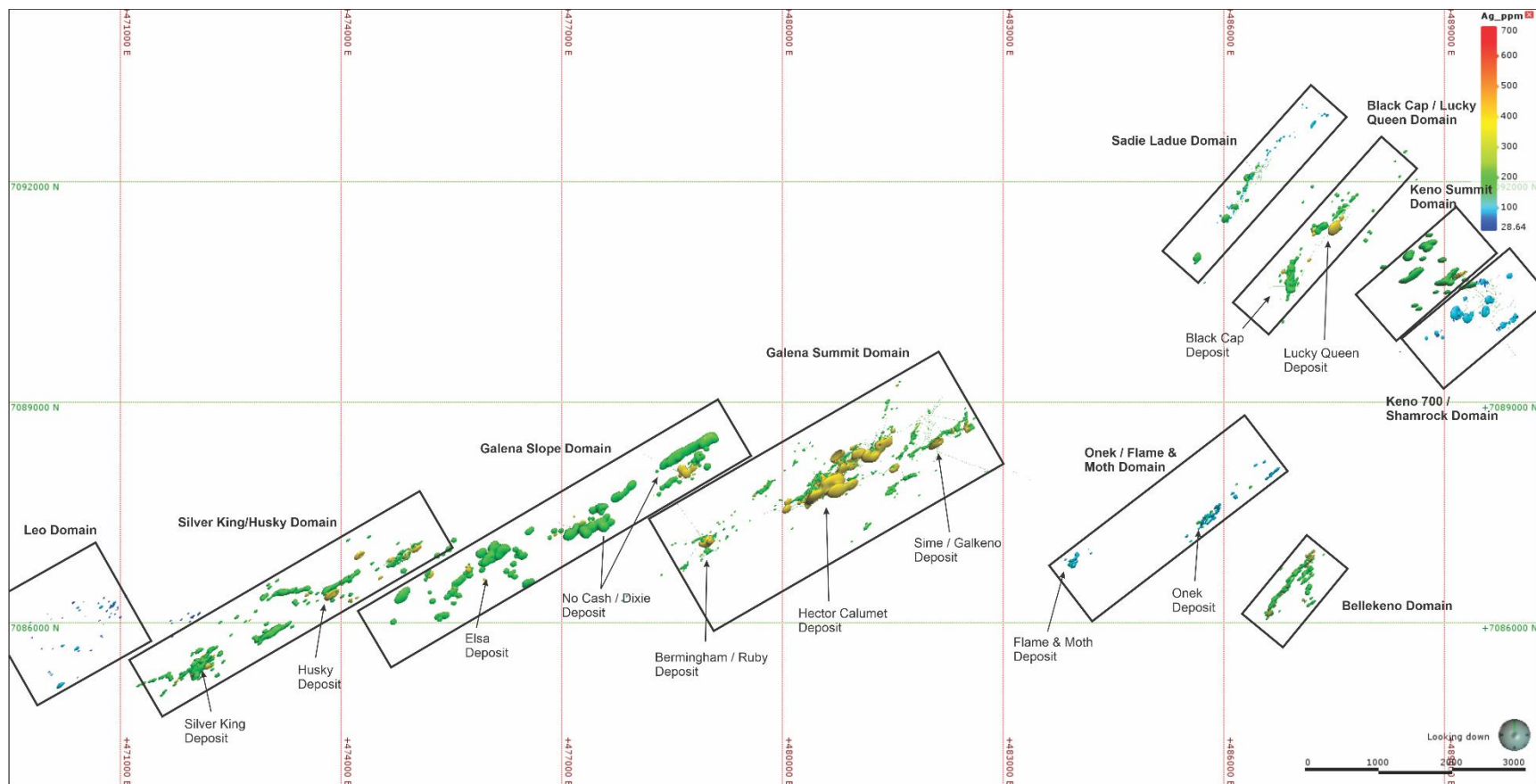


**Figure A.6: Map showing locations of mineralised domains.**

### ***Descriptions and Uses of Grade Modelling Functions in Leapfrog Geo<sup>TM</sup> Software***

Leapfrog Geo<sup>TM</sup> allows users to define isotropic grade boundaries from borehole assay data to produce estimated volumes of equal grade (grade shells). To define these volumes Leapfrog Geo<sup>TM</sup> uses a conditional probability method to produce dynamic implicit models (Spragg, 2013b). The software uses a fast radial basis function (FastRBF<sup>TM</sup>) to interpolate data to produce isosurfaces delineating calculated volumes of equal grade distribution (Carr et al., 2001). The FastRBF<sup>TM</sup> populates the whole 3D volume with an interpolated mathematical function so that spatial queries can be calculated within the volume of the model that would otherwise be impossible (i.e., evaluation of grade onto structure surfaces; Hill et al., 2014). Interpolation is a method that produces an estimate or “interpolated value” of a quantity that is not known at a given point, but is known at other points, such as from drillhole data (Figure A.7 and Figure A.8). With guidance from the user Leapfrog Geo<sup>TM</sup> uses FastRBF<sup>TM</sup> to “interpolate” or fill in the gaps where there is no data (Spragg, 2013b).

Two interpolants are available in Leapfrog Geo<sup>TM</sup>; these are the *linear* and *spheroidal interpolants* (Figure A.8). The interpolant defines a weighting to give each sample based on its distance from the point X (Figure A.7 and Figure A.8; Spragg, 2013b). This weighting is inversely proportional to distance from the estimation point X (McLennan, 2013).

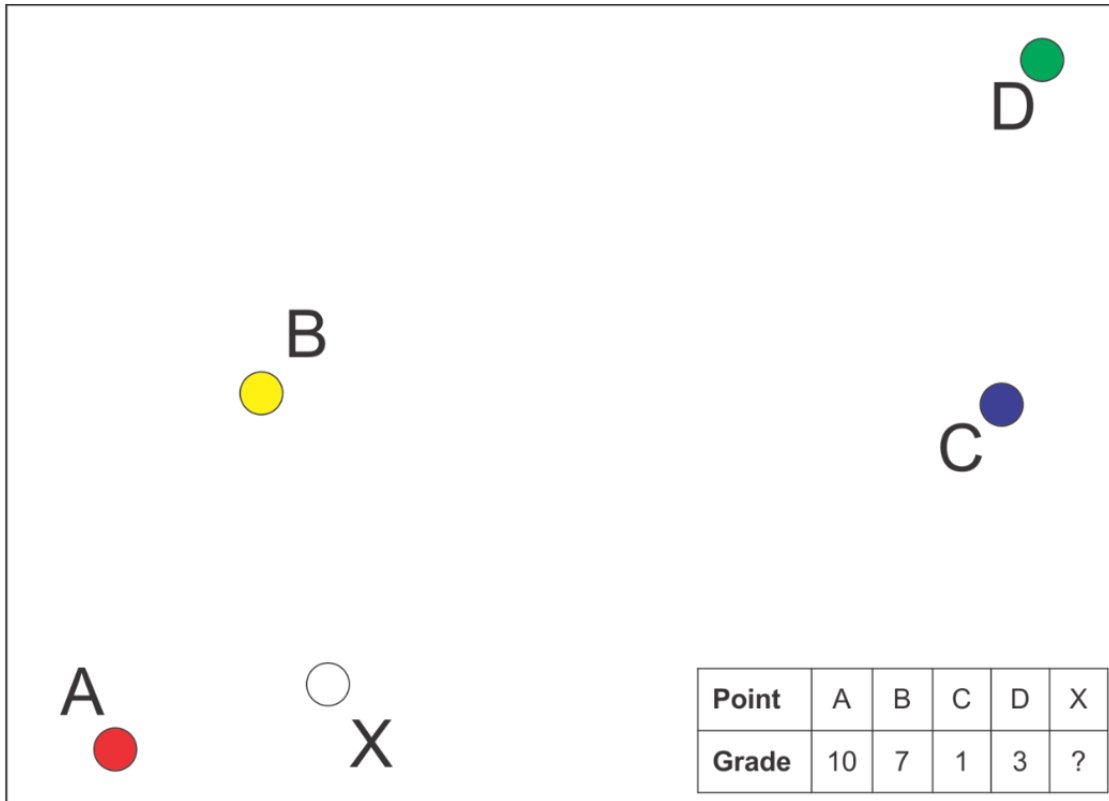


**Figure A.7: Hypothetical map where the grades of points A to D are known and the grade at point X is unknown (modified from Spragg, 2013b).**

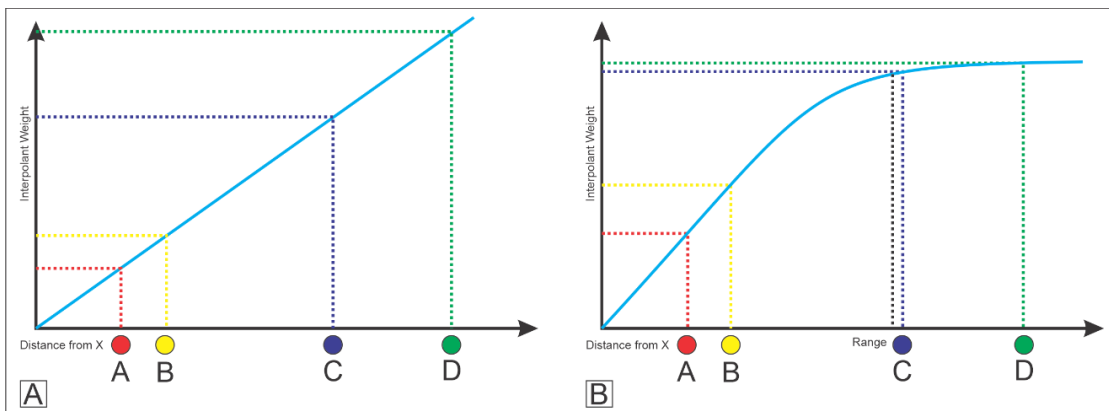


**Figure A.8: Linear (A) and spheroidal (B) interpolant graphs for hypothetical map in Figure A.7 (modified from Spragg, 2013b) .**

All interpolant functions pass through or close to two points defined by three common parameters. The points are (0.0, n) and (r, s), where n, r, and s are the *nugget*, *range*, and *sill* parameters, respectively (Spragg, 2013b). The *nugget*, *range*, and *sill* parameters can all be manually attributed by the user (Figure A.9):

- *Nugget* represents a local anomaly in sampled values that is substantially different from what would be predicted at that point, based on the surrounding data;
- *Sill* defines the upper limit of the spheroidal interpolant function where there ceases to be any correlation between values. The sill is asymptotic, thus as the distance increases, the value of the function approaches the sill;
- *Range* is the distance at which the interpolant is 96% of the sill (with no *nugget*).

The *linear interpolant* assumes that known data closer to point X is more important than data that is far away and estimates produced will strongly reflect values at nearby points. When using the *linear interpolant*, the estimate is always influenced most by the closest sample points. This is still the case even when all the samples are a great distance from the estimation point (Spragg, 2013b). The *linear interpolant* is a good general purpose model and works well for lithology data, which often has localised pockets of high resolution data. It is not appropriate for values with a distinct finite range of influence as it aggressively extrapolates out from the data. Most grade data is not well interpolated using a *linear interpolant* function (McLennan, 2013).



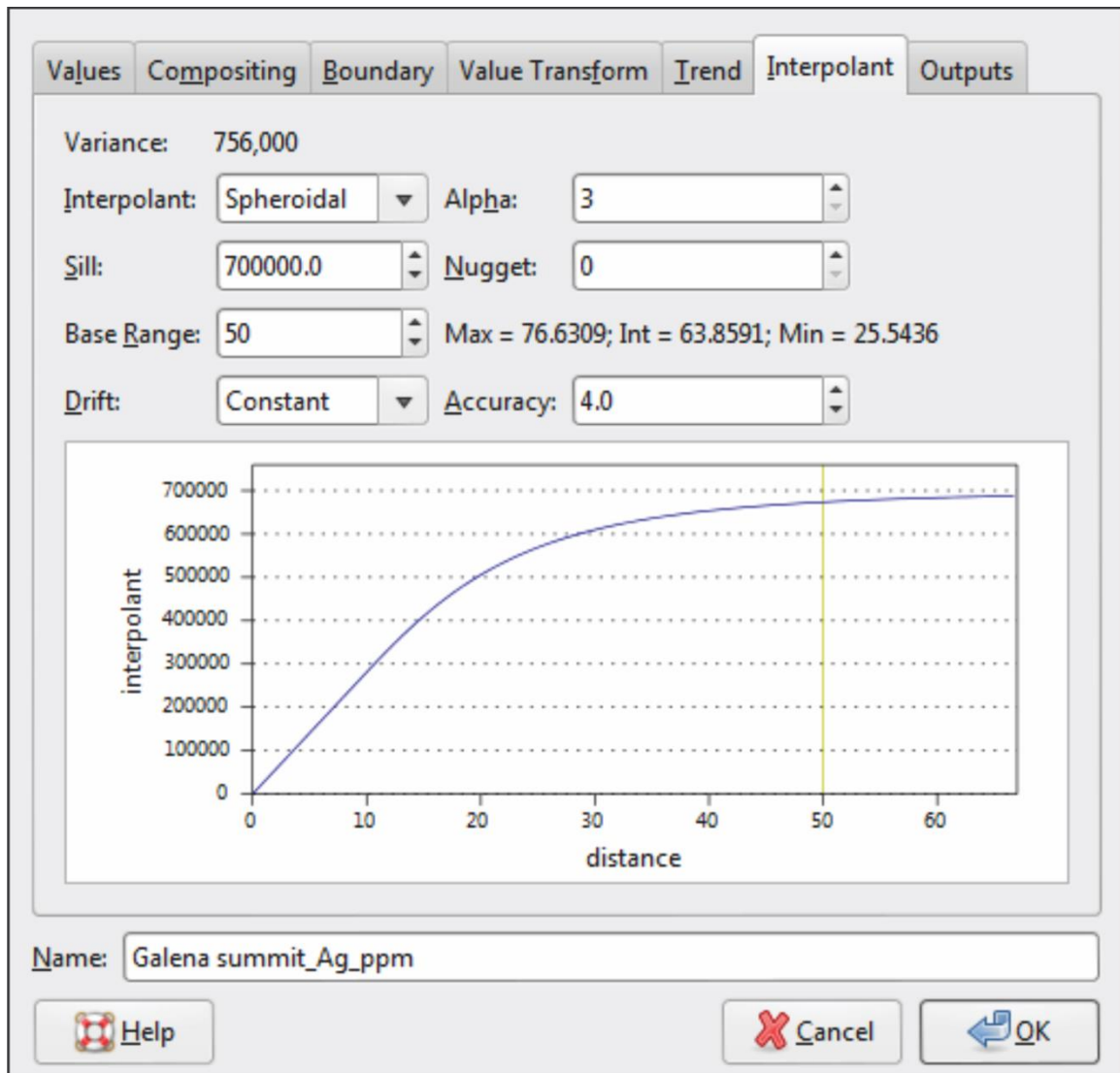


Figure A.9: Screen capture of the Leapfrog Geo™ interpolant user interface.

The *spheroidal interpolant* flattens out at a given distance (*range*) from point X (Figure A.8 and Figure A.9). Sample locations that are within the *range* are assigned an importance, based on their distance from X in the same way as in the *linear interpolant* method. Samples whose distance from X exceeds the *range* are assigned roughly the same importance and will have approximately the same influence on the estimate no

matter their distance away (Spragg, 2013b). As such, the low-grade value at D (Figure A.7 and Figure A.8) will have more of an influence on the estimated value than before and the estimated value for X should be smaller (Spragg, 2013b).

In addition to the interpolation functions, the *Global Trend* and *Structural Trend* tools are available that allow control over the continuity of interpolant grade. The *Global Trend* is suitable in situations where the underlying geology implies that grade is continuous in a planar direction over large distances. While the *Structural Trend* function is more appropriate for more complex systems.

The *Global Trend* defines a constant trend that to be used by the interpolant and will estimate grade continuity in one direction across the model. The extent to which one direction is favoured over others is defined by the relative sizes of ellipsoid ratios; that is, the direction with the largest ratio is favoured more than the others, while the direction with the smallest is favoured least (Figure A.10 and Figure A.11; Spragg, 2013a).

The *Structural Trend* function is an advanced version of the *Global Trend* function that allows changes in direction of grade continuity over a defined surface. While the *Global Trend* function is based on the orientation and defined ellipsoid ratios of a plane, the *Structural Trend* function is directly associated with user built and defined surfaces or meshes (i.e., fault surfaces, foliation, or lithological breaks). The surface is effectively downsampled to determine the local trend at each point on the mesh to generate an anisotropy that varies throughout the defined space (Joynt, 2013). The *Structural Trend*

does not determine the final surface; this is still done by the interpolant and the data points used.

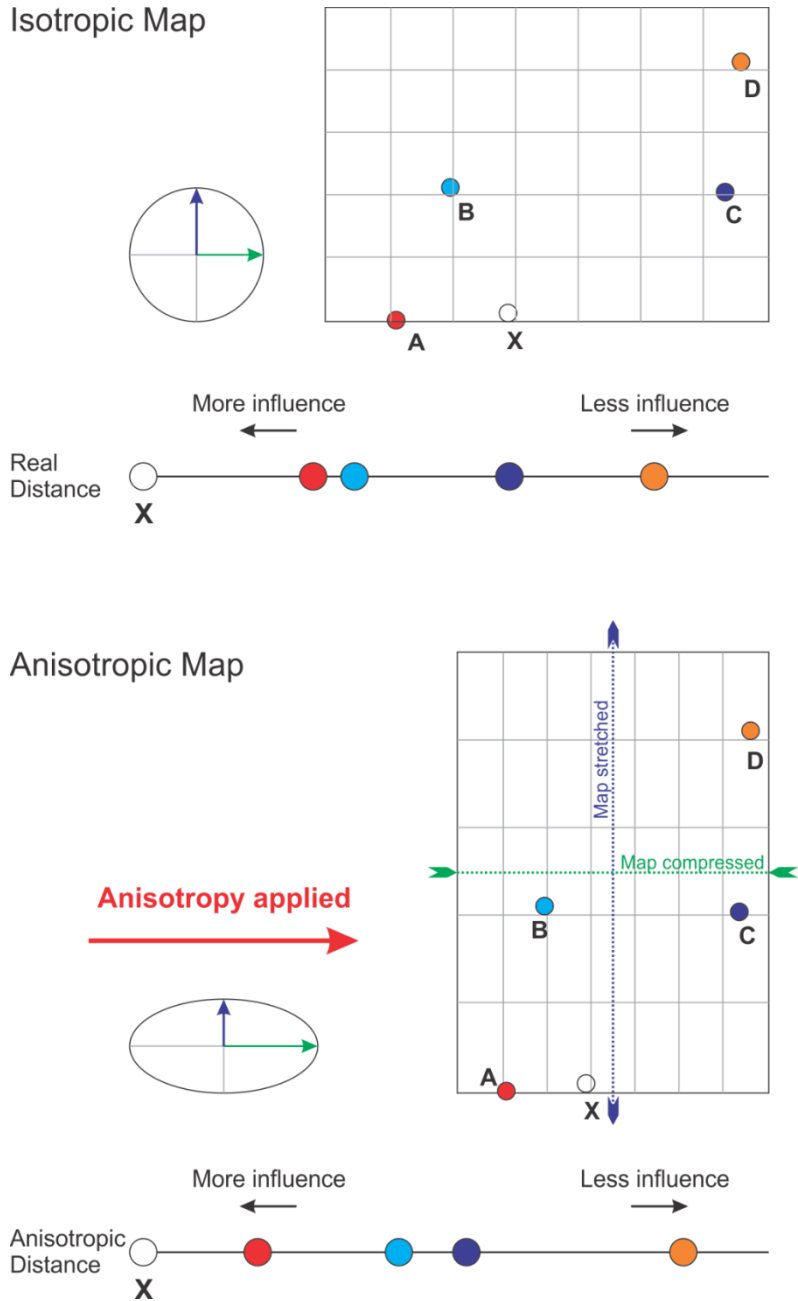


**Figure A.10: Hypothetical map showing the influence of isotropic (top) and anisotropic (bottom) interpolants to the estimate of unknown sample (X) from known samples (A to D) (modified from Spragg, 2013b).**

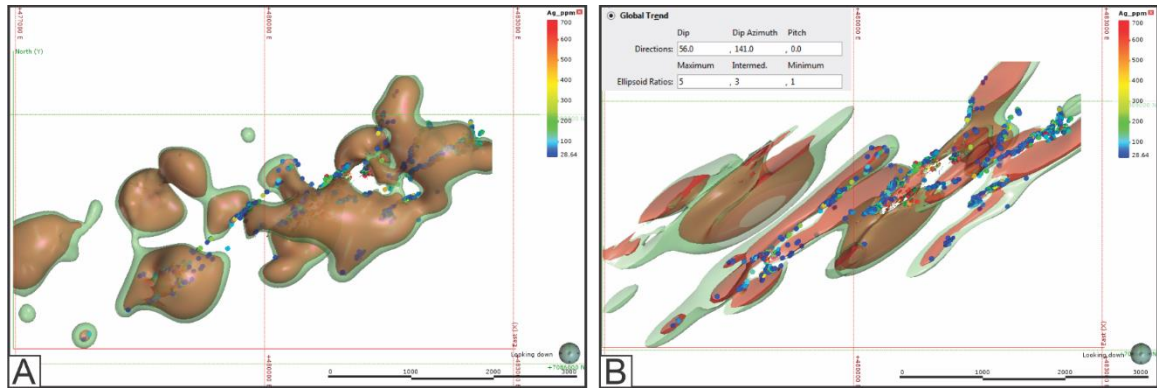


**Figure A.11: Plan view examples of isotropic (A) and anisotropic (B) Ag grade interpolation from the Calumet deposit. Anisotropic interpolation has a *Global Trend* applied dipping 56° towards 141°, with maximum:intermediate:minimum ellipsoid ratios of 5:3:1. Grade isoshells: Green > 200 g/t Ag; Red > 600 g/t Ag.**

Leapfrog Geo™ has three different types of *Structural Trend*, with each behaving slightly differently. These are *non-decaying*, *blended*, and *strongest-along-meshes* trends.

All of the trends are controlled by a user-defined *strength* and *range*:

- *Strength* dictates how much elongation can be applied in a given direction;
- *Range* is the distance from the mesh in which the trend has an effect.

*Non-decaying* meshes are similar to *Global Trends* in that they have an influence across the entire model but can be built from a mesh or meshes of any shape (Figure A.12A).

*Blended* trends allow users to build a trend from multiple meshes specifying a *range* and *strength* for each mesh (Figure A.12B). If two or more of the trends intersect each other, a combined trend is calculated. The *strongest-along-meshes* trend allows users to create multiple trends that decay in *strength* back to the estimated *Global Trend* of the data based on a set *range* (Figure A.12C).

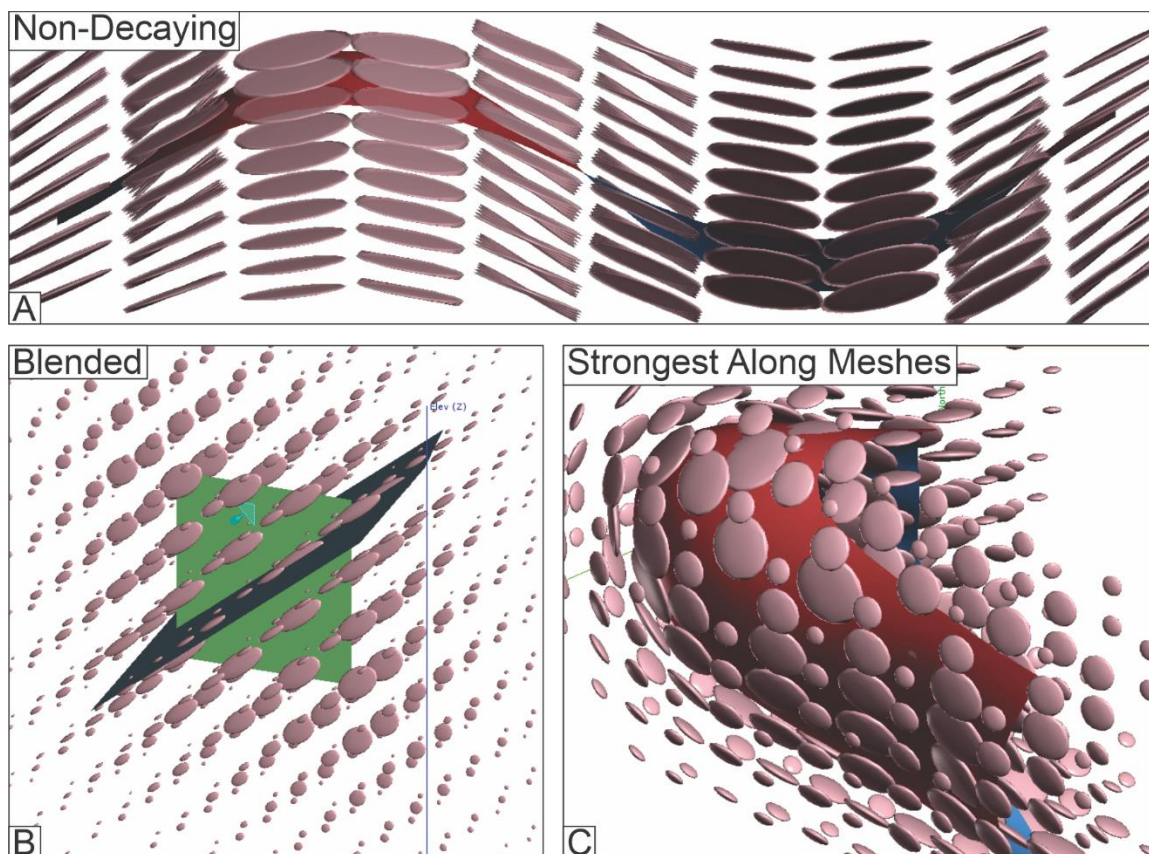


**Figure A.12: Schematic examples of structural trend types available in Leapfrog Geo™. Discs around meshes show trend of interpolant and disc size shows relative strength of interpolant.**

A: *Non-decaying* structural trend; B: *Blended* structural trend, with green and blue meshes used to define trend. Proximal to a single mesh the trend is subparallel to that mesh; proximal to the intersection of the meshes the trends of the individual meshes are combined. Note that interpolant decays to an isotropic trend with distance from the meshes; C: *Strongest-along-meshes* trend whereby the interpolant is controlled by the geometry of the mesh and decays to an isotropic, or defined global trend at a defined range from the mesh.

### ***Application of Grade Modelling Functions to the Keno Hill Dataset***

For this project, test grade isoshells were produced for each domain (Figure A.6). The grade shells were calculated for Ag in grams per tonne. The isosurfaces produced were dependant upon the recorded grade in each individual domain or mineralised trend; however, grade isoshells were typically produced for 100, 200, 500, and 1,000 g/t.

Numerous variations of the grade modelling methods outlined above were tested; however, due to the fault-controlled character of Ag-Pb-Zn mineralisation within the Keno Hill district, the *strongest-along-meshes* interpolant was used to interpolate the assay data (Figure A.13). Meshes were built from polylines and structural data and were based on field measurements of major Ag-Pb-Zn-bearing faults, digitised level plan data, airborne magnetic data, and from the observed trend of Ag borehole assay data. A background *Global Trend* was calculated from the average orientation of all faults in the domain. All grade shell interpolants decayed to this orientation over a *range* that was dependant on the amount and quality of the data supplied.

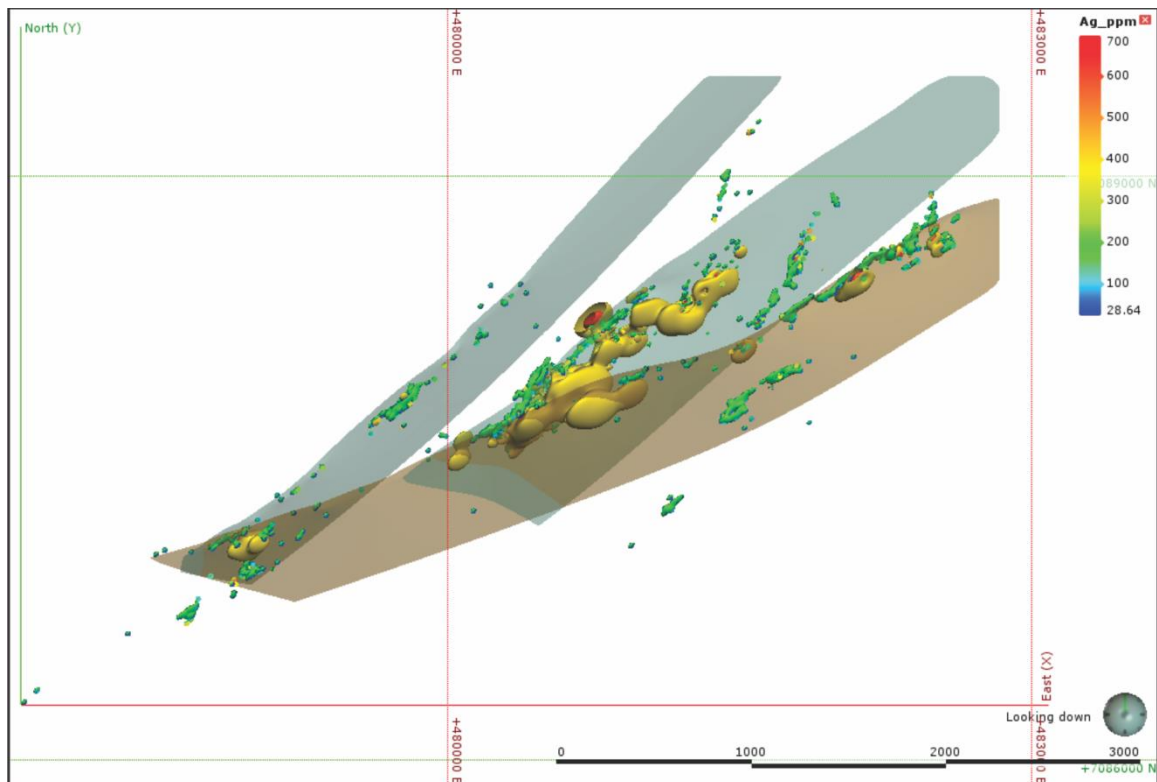


**Figure A.13:** Plan view example of meshes (blue and brown) used for *strongest-along-meshes* interpolant in the Calumet deposit. Grade isoshells: Green > 200 g/t Ag; Yellow > 400 g/t Ag; Red > 600 g/t Ag.

The Galena summit area has a large amount of good quality data available. As such, it was selected to construct a detailed vein model. The methodology for building the vein model is described below, but here it should be noted that subsequent to the domain-scale, unrestricted Ag grade modelling, Ag grade was modelled exclusively within modelled veins. The modelled veins were combined as a single output volume, and a *multi-domain RBF* interpolant was applied to the volume. This process restricts the interpolant to estimating assay data that occurs solely within the modelled vein output volume. The same *Structural Trend* that was applied to the domain-scale interpolant was applied to the *multi-domain RBF* interpolant.

#### **A.6.2.2 Fault and Vein Modelling**

##### ***Descriptions of Fault and Vein Modelling Functions in Leapfrog Geo<sup>TM</sup> Software***

The Leapfrog Geo<sup>TM</sup> *Geological Model (GM)* function includes features that enable the user to model structural features including the *fault system* and *vein system* functions. The *fault system* function allows faults to be built from various input data, and for a fault history to be defined. Older faults can be truncated by younger, cross-cutting faults. If an older fault is segmented by a younger, cross-cutting fault, then a discrete fault must be built for each segment, however the same data inputs may be used. The result of defining a fault history is that Leapfrog Geo<sup>TM</sup> creates a series of fault blocks that can subsequently be used for lithology, grade, or additional structural modelling.

While faults are complex, three-dimensional zones that comprise multiple, linked slip surfaces, Leapfrog Geo™ does not allow for faults to be assigned a width, as such the faults modelled using the *fault system* function are two-dimensional surfaces. This does not allow for analysis of variations in fault width, or analysis of Ag grade as a function of fault width. As such the *vein system* function was used to model Ag-Pb-Zn-mineralised (D<sub>2</sub>) faults. The *vein system* function effectively mimics the *fault system* function, whereby a vein history can be defined; however, veins must have a width defined by data or by the user, and fault blocks are not defined by individual veins. Veins will cut across all units and structures within the model, unless they are specifically truncated by a subsequent user defined fault, vein, or erosional surface. To define a vein the *interval selection* tool can be used to select drill core intervals and then build a volume from their contact points. The volumes can be modified by using GIS vector data, polylines, or point data.

### ***Application of Fault and Vein Modelling Functions to the Galena Hill Summit***

#### ***Domain***

The *fault system function* was used to build the post-mineralisation (D<sub>3</sub>) fault architecture and the *vein system function* was used to build the D<sub>2</sub> architecture. No pre-mineralisation (D<sub>1</sub>) structures were modelled.



Borehole data, surficial mapping data, lineament interpretations, and infrastructure wireframes .dxf files were available to the author in the NAD83 UTM zone 8N datum, and as such could be directly imported into Leapfrog Geo™, however the historic level plans were supplied as non-georeferenced, scanned, hand drawn images that were projected on a local mine grid. The level plans were imported into ArcGIS™ software, aligned to the historic infrastructure and georeferenced. The level plans were digitized in ArcGIS™ and the resultant shapefiles were imported into Leapfrog Geo™ as vector files to help guide the modelling process.

D<sub>3</sub> faults were built first, using the *fault system* tool:

- The orientation and surface trace of D<sub>3</sub> faults were identified from surficial mapping data, orthographic photos (Figure A.14), and the DEM lineament interpretation, and to a lesser extent the interpretation of magnetic data. Magnetic data was used sparingly because the depth of magnetic response is unknown. Polyline of the surficial trace were drawn on the topography and structural data were added at point of measured fault orientation.
- Faults were projected to depth to check for correlation with D<sub>3</sub> faults from digitized level plans. If correlation was observed polyline was added to define the structure at depth.
- Offsets in lithology and Ag grade were identified to guide fault geometry (Figure A.15).
- Modelled D<sub>3</sub> faults were assigned an age relative to other modelled D<sub>3</sub> faults and cross-cutting relationships were defined. The faults were made active in Leapfrog

Geo<sup>TM</sup> to produce a series of fault blocks, into which D<sub>2</sub> faults/veins would be modelled.

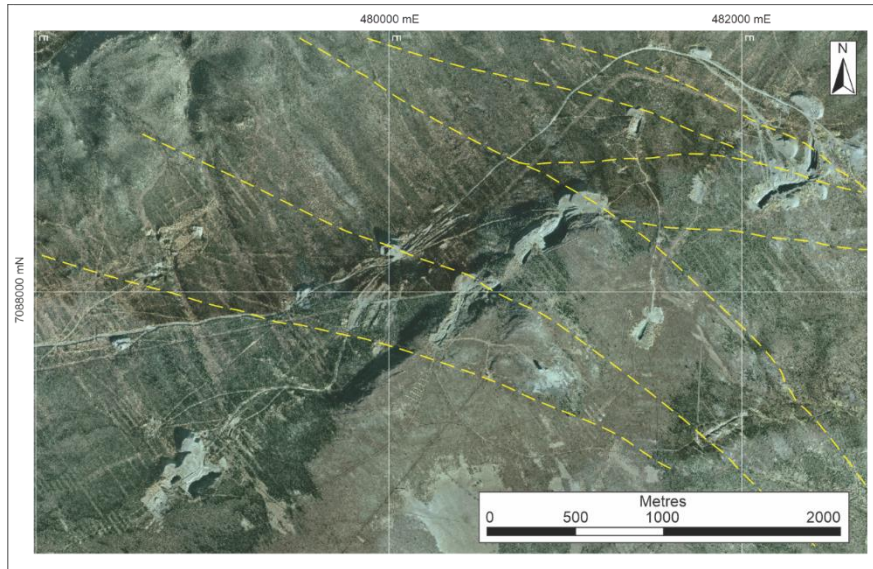


**Figure A.14:** Orthophotograph data showing surface traces of modelled D<sub>3</sub> faults in the Galena summit domain.

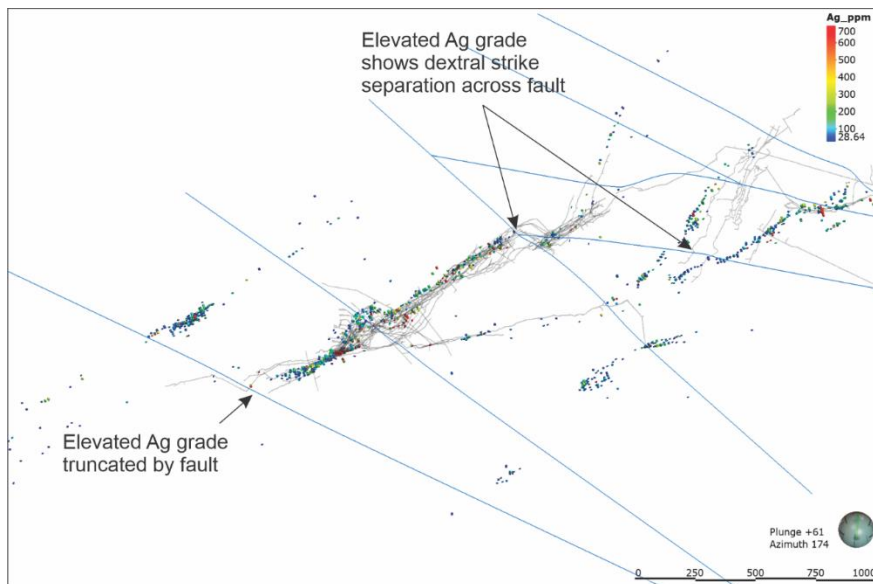


**Figure A.15:** Inclined slice showing trace of modelled D<sub>3</sub> faults (blue), Ag assay data, and subsurface infrastructure (grey) in the Galena summit domain. Elevation of slice at centre of image approximately 1155 masl.

D<sub>2</sub> veins were modelled as *vein systems* by identifying trends in assay data, and by using the *interval selection* tool:

- The assay data were displayed in 3D and then sliced as cross-sections perpendicular to the observed mineralisation trend, as down-dip sections, or as plan view sections.
- Stepping through the model, assay intervals were selected that were considered to belong to specific structures (Figure A.16).
- Polylines or structural point data were added to either vein footwalls or hanging walls at known vein boundaries.
- Veins were modified by selecting individual assay intervals and assigning their contacts to the vein footwall, or hanging wall, or excluding them from the interpretation.
- The modelled veins were assigned to a vein system, and cross-cutting or truncation relationships were defined relative to other modelled veins.
- This process was repeated for each modelled vein within each fault block defined by the modelled D<sub>3</sub> faults.
- Finally, all *vein systems* were assigned to the same lithological code. As such, a single output volume could be built from the *vein systems*. This allowed for a *multi-domain RBF* interpolant of Ag grade to be estimated for the entire modelled *vein system* (Figure A.17).

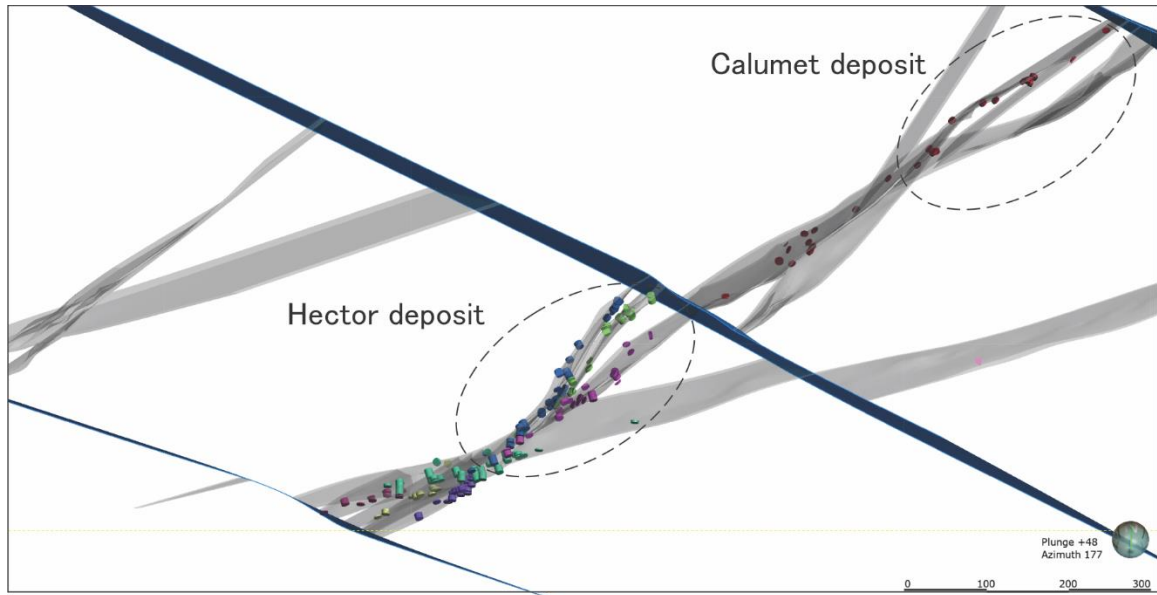


**Figure A.16: Inclined slice through Hector and Calumet deposits showing interval selection for selected modelled veins. Grey: modelled D<sub>2</sub> vein system; Blue: modelled D<sub>3</sub> faults.**

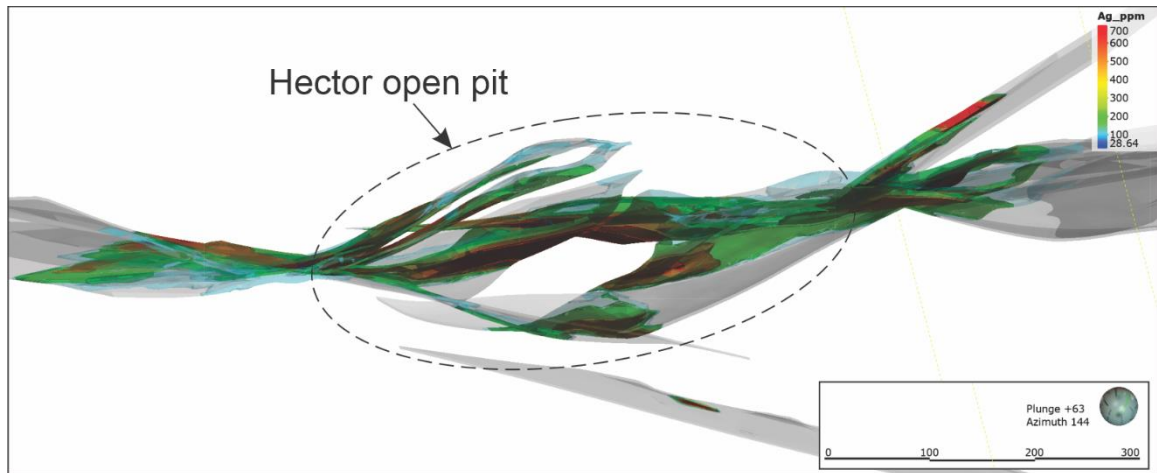


**Figure A.17: Inclined view of vein system model (gray) at the Hector deposit.**

Grade isoshells use strongest along meshes trend, and multi-domain RBF interpolant to restrict grade estimation to vein system model. Grade isoshells: light blue > 100 g/t Ag; green > 200 g/t Ag; orange > 500 g/t Ag; red > 1000 g/t Ag.

## **A.7 Laboratory Analytical Techniques**

During the field investigations 226 samples were collected (Appendix C). 93 polished thin sections and 34 polished slabs were prepared for further petrographic, geochemical, and analysis (Appendix E). In addition, 6 whole rock samples were analysed for geochronological analysis by the U-Pb and  $^{40}\text{Ar}/^{39}\text{Ar}$  methods (Appendix F). The following section outlines the procedures employed for each analytical technique.

### **A.7.1 Optical and Scanning Electron Microscopy**

The 93 polished thin sections were prepared at the University of New Brunswick (UNB) and were analysed using a binocular optical microscope. Samples were analysed under plane polarised light, cross-polarised light, and reflected light. Selected samples were scanned at various scales using a Zeiss Axio Imager A1m microscope, and images were stitched together to produce high-resolution photomicrographs using Zeiss AxioVision<sup>TM</sup> software.

Samples were analysed for mineralogy, structural fabrics and textures, and additional areas of interest within polished thin sections were identified for further analysis by scanning electron microscope (SEM). The high image resolution of scanning electron microscopy allows for analysis features in a range of millimeters down to a few nanometers. The polished thin sections selected for SEM-EDS analysis were assessed

under a binocular microscope, areas of interest were marked, and the sections were carbon coated.

A total of eight thin sections were analysed by SEM (Appendix C). Six samples were analysed using a JEOL JSM6400 Digital SEM, equipped with Geller dPict digital image acquisition software, and an EDAX (Genesis) Energy Dispersive X-ray Analyzer at UNB's Microscopy and Microanalysis Facility (MMF). The JEOL 6400 SEM has a tungsten filament that, when heated, emits electrons which are accelerated down through the column. Electromagnetic lenses in the column direct and focus the electron beam so that the "spot size" (the diameter of the electron beam at the specimen) decreases from ~50 microns to ~10 microns, or approximate x5000 magnification (ACMAL, 2014). Qualitative and quantitative compositional analysis can be acquired using the EDAX (Genesis) Energy Dispersive X-ray Analyzer.

Four samples were analysed using a Hitachi SU-70 Field Emission Gun (FEG) SEM at UNB's Planetary and Space Science Centre (PASSC) including two samples that had previously been analysed using the JEOL 6400 SEM. The Hitachi SU-70 (FEG) SEM can perform ultra-high resolution scanning electron microscopy at the nanometre scale. It is equipped with a Schottky thermal emitter that can acquire ultra-high-resolution images (1.0 nm/15kV, 1.6nm/1 kV), and an Energy Dispersive Spectrometer (EDS) that is used to determine the chemical composition of materials.

### **A.7.2 Geochemical Analysis**

Twenty-eight field and drill core samples were selected for geochemical analysis (Appendix E). Geochemical analytical techniques included instrumental neutron activation analysis (INAA; 21 samples), X-ray diffraction (XRD; 21 samples), and X-ray Fluorescence Spectrometry (XRF; 28 samples). Twenty-one samples of variably deformed greenstone were analysed by the INAA, XRD, and XRF methods; seven additional samples were analysed by the XRF method alone. Below is a brief description of the scientific basis for each method.

INAA is a sensitive, non-destructive analytical method that has the potential to determine the concentration of up to 40 elements, simultaneously, in the ppb–ppm range in a wide variety of materials (Eby, 2013). The INAA analysis produced concentration data for 35 major and minor elements. ActLabs provided the detection limits calculated for the 35 elements (Table A.4).

**Table A.4: Detection limits for INAA data as provided by ActLabs. Data sorted by highest precision.**

<b>Element</b>	<b>INAA Detection Limit</b>
Au	2 ppb
Ir	5 ppb
Fe	0.01 ppm
Lu	0.05 ppm
Sb	0.1 ppm
Sc	0.1 ppm
Sm	0.1 ppm
Th	0.2 ppm
Eu	0.2 ppm
Yb	0.2 ppm
As	0.5 ppm
Br	0.5 ppm
Ta	0.5 ppm
U	0.5 ppm
La	0.5 ppm
Tb	0.5 ppm
Co	1 ppm
Cs	1 ppm
Hf	1 ppm
Hg	1 ppm
Mo	1 ppm
W	1 ppm
Se	3 ppm
Ce	3 ppm
Ag	5 ppm
Cr	5 ppm
Nd	5 ppm
Rb	15 ppm
Ni	20 ppm
Ba	50 ppm
Zn	50 ppm
Na	0.01 wt. %
Sn	0.02 wt. %
Sr	0.05 wt. %
Ca	1 wt. %

INAA is typically dependant on measuring gamma radiation induced in a sample by irradiation with neutrons (Hoffman, 1992). Commonly, samples are encapsulated and irradiated in a nuclear reactor for between one and four hours depending on neutron flux and the amount of material (Eby, 2013). During irradiation, a thermal neutron is captured by a target nucleus increasing its atomic mass by 1 (Hoffman, 1992; Eby, 2013). This results in a radioactive nucleus that decays to a stable form by the emission of a beta



particle and the emission of gamma rays (Eby, 2013). Each radioactive nuclide decays with a specific half life and emits gamma rays of a characteristic energy or “fingerprint” (Hoffman, 1992). The half lives of the nuclides are typically extremely short, on the order of milliseconds, and it is the decay gamma rays that measured and quantified by INAA (Hoffman, 1992). After a suitable decay period the samples are measured instrumentally on a high-resolution germanium (Ge) detector (Hoffman, 1992; Eby, 2013). The characteristic gamma rays are used to determine the isotope and their intensities are used to determine the absolute concentrations (Eby, 2013).

XRD analysis is a fast analytical, non-destructive technique that can provide information on phase identification, texture, grain size, crystallinity, strain, and defects of crystalline material and determine their average bulk composition (Kohli and Mittal, 2019; Dutrow and Clark, 2020). The XRD analysis was conducted on a Bruker D8 Advance at UNB. The technique is based on the constructive interference of monochromatic X-rays and a crystalline sample (Dutrow and Clark, 2020). The X-rays are produced by a cathode ray tube, filtered, collimated, and directed towards the sample (Dutrow and Clark, 2020) where they are scattered at angles specific to each set of lattice planes in the sample (Kohli and Mittal, 2019). The technique is based on Bragg’s Law where diffraction is described as the reflection of an X-ray beam by crystallographic planes defined by the indices  $hkl$  (Lavina et al., 2014). Bragg’s law is expressed as:

$$2d_{hkl}\sin\theta_{hkl} = n\lambda$$

where  $n$  (an integer) is the “order” of reflection,  $\lambda$  is the wavelength of the incident X-rays,  $d$  is the interplanar spacing of the crystal and  $\theta$  is the angle of incidence (Henry et

al., 2016). The sample is rotated by  $\theta$  and the detector is rotated by  $2\theta$  so that all possible diffraction directions of the lattice are attained. The produced X-ray spectra are detected and the conversion of the peaks to  $d$ -spacing is calculated using Bragg's law (Lavina et al., 2014). Each mineral has a unique set of  $d$ -spacings, and as such comparison of  $d$ -spacings to standard reference patterns allows for mineral identification.

XRF spectrometry is a widely used technique to determine the concentrations of major and geochemically important trace elements in geological samples (Potts and Webb, 1992). In XRF spectrometry samples are excited by a beam of X-rays (incident beam) resulting in the ionisation of inner shell orbital electrons by the photo-electric effect (Potts and Webb, 1992). During this process some electrons are scattered, and some are absorbed into the material. The manner in which electrons are scattered or absorbed is dependant on the sample's chemistry (Wirth and Barth, 2020). Excitation and ionisation cause the electronic structure of the atom to become unstable and decay almost instantaneously to a more stable electronic configuration (Potts and Webb, 1992). The particle energy released during this process is lower than the incident radiation and is termed fluorescent radiation (Wirth and Barth, 2020). The energy emitted is characteristic of a transition between specific electron orbitals, and as such analysis of the emitted x-ray spectrum can be used to calculate concentrations of elements within the sample (Wirth and Barth, 2020).

### **A.7.3 Geochronological Analysis**

6 rock samples were selected for geochronological analysis (Appendix F). Five whole rock samples were selected for  $^{40}\text{Ar}/^{39}\text{Ar}$  analysis; one whole rock sample was selected for U-Pb CA-TIMS (Chemical Abrasion - Thermal Ionization Mass Spectrometry) analysis. Below is a brief description of the scientific basis for each method and their application in this thesis.

#### **A.7.3.1 $^{40}\text{Ar}/^{39}\text{Ar}$ Analysis – Scientific Basis**

The basis of  $^{40}\text{Ar}/^{39}\text{Ar}$  dating lies in the K/Ar radiometric dating method. Potassium (K) is the eighth most abundant element in the earth's crust comprising about 1 wt% (McDougall and Harrison, 1999) and is a major component of many rock-forming minerals, with biotite, muscovite and K-feldspar containing weight percent levels of K. Three isotopes of K exist naturally:  $^{39}\text{K}$  and  $^{41}\text{K}$  are stable and  $^{40}\text{K}$  is radioactive (e.g., Faure and Mensing, 2005). In addition, there are three naturally occurring isotopes of Ar:  $^{40}\text{Ar}$ ,  $^{38}\text{Ar}$ , and  $^{36}\text{Ar}$  (McDougall and Harrison, 1999).  $^{40}\text{K}$  follows a branched or dual decay path whereby 89.52% of the time  $^{40}\text{K}$  decays to  $^{40}\text{Ca}$  and 10.48% of time it decays by extranuclear electron capture to  $^{40}\text{Ar}$  (Marshall, 1998).

Potassium is the eighth most abundant element in the earth's crust with  $^{40}\text{K}$  comprising about 0.012% of all naturally occurring K. Its abundance and half life of around 1.25 Ga

(Bowen, 2011) makes it ideal for use as a geochronometer. However, there are two principal issues with the K/Ar dating method. First is that quantitative analysis of both K and Ar cannot take place in the same machine; the second is that there is some ambiguity in the source of the measured Ar, be it atmospheric or radiogenic. The advantage of the  $^{40}\text{Ar}/^{39}\text{Ar}$  technique is ability to determine the composition of an extraneous Ar reservoir and correct for it (McDougall and Harrison, 1999).

Wänke and König (1959) showed that after irradiating samples in a nuclear reactor, interactions with neutrons caused a proportion of  $^{39}\text{K}$  to transform to  $^{39}\text{Ar}$  (designated  $^{39}\text{Ar}_\text{K}$ ). Merrihue (1965) showed that the amount of  $^{39}\text{Ar}_\text{K}$  generated could be measured by mass spectroscopy. Because the  $^{39}\text{K}/^{40}\text{K}$  ratio in nature is essentially constant, if one is able to measure the efficiency of the transformation in the reactor we can use  $^{39}\text{Ar}_\text{K}$  as a proxy for  $^{40}\text{K}$ . In addition, because  $^{39}\text{Ar}$  does not occur naturally, inheritance or atmospheric contamination is not a concern.

Megrue (1973) reported the use of a focused, pulsed laser beam to release argon by ablation from a localized area of a sample ( $\sim 100\text{ }\mu\text{m}$ ), while York et al. (1981) used a continuous wave (cw) argon ion laser beam to fuse a sample directly. Total fusion  $^{40}\text{Ar}/^{39}\text{Ar}$  ages could be measured on very small sample or individual crystals, and a defocused cw-beam could be used to progressively step heat a sample to produce age spectra. Step heating a sample initially, at low temperatures, releases loosely bound Ar from the crystal (possibly Ar adsorbed to the crystal surface or near surface). Increasing temperatures releases Ar that is more tightly bound to the crystal structure (McDougall

and Harrison, 1999). Analysis of inverse isochron diagrams produced by step heating can determine the composition of extraneous Ar. Correcting for this result can reveal the true age of the sample. However, while radiogenic Ar has a large atomic size (1.9Å; McDougall and Harrison, 1999), increased temperature will cause loss of radiogenic argon by diffusive transfer and as such the age will only give an age of cooling below a critical blocking temperature for Ar diffusion.

Due to the abundance of K in the earth's crust many K-bearing minerals can be used to radiometrically date rocks. For this project five whole rock samples were selected for  $^{40}\text{Ar}/^{39}\text{Ar}$  analysis. The analysis was performed on samples of sericite from the selvage of Ag-Pb-Zn mineralised veins, in an attempt to determine the timing of mineralization and hydrothermal alteration. Sericite is a fine-grained variety of white (colourless) to pale green mica, that is mainly composed of muscovite, illite or rarely paragonite. Muscovite has an ideal composition of  $\text{K}_2\text{Al}_4\text{Si}_6\text{Al}_2\text{O}_{20}(\text{OH},\text{F})_4$  that permits 9 % of K in its structure (McDougall and Harrison, 1999). Muscovite is common in regionally metamorphosed rocks, is stable over a wide range of temperature and pressure conditions and shows good radiogenic Ar retention properties with a closure temperature of around 350° C for moderate cooling rates (McDougall and Harrison, 1999).

### *<sup>40</sup>Ar/<sup>39</sup>Ar Analytical Methodology Used in Preparation of this Thesis*

Samples for <sup>40</sup>Ar/<sup>39</sup>Ar analysis were collected at (Ag)Pb-Zn-mineralised vein selvages in drill core and from the 750-1 crosscut in the Bellekeno underground mine (samples 0187-005, U0160-009, and K-BX-007), and in strongly sericite-altered rocks within the fault damage zone associated with the Onek vein. The details for procedure used for the <sup>40</sup>Ar/<sup>39</sup>Ar analysis were provided by D. Archibald (personal communication, February 10, 2012) and are paraphrased below.

Mineral separates and flux-monitors (standards) were irradiated with fast neutrons in position 5C of the McMaster Nuclear Reactor (Hamilton, Ontario) for a duration of 9 h (at 3 MWH). For step-heating, the laser beam of a 30W New Wave Research MIR 10-30 CO<sub>2</sub> laser is defocused to 2 mm to cover the entire sample. Heating periods are ca. 3 minutes at increasing percent power settings (1.5 to 7 %). The evolved gas, after purification is admitted to an on-line, MAP 216 mass spectrometer, with a B ur Signer source and an electron multiplier (set to a gain of 100 over the Faraday detector). Blanks, measured routinely, are subtracted from the subsequent sample gas-fractions (D. Archibald personal, communication, February 10, 2012).

Measured argon-isotope peak heights are extrapolated to zero-time, normalized to the <sup>40</sup>Ar/<sup>36</sup>Ar atmospheric ratio (295.5) using measured values of atmospheric argon, and corrected for neutron-induced <sup>40</sup>Ar from potassium, <sup>39</sup>Ar and <sup>36</sup>Ar from calcium, and <sup>36</sup>Ar from chlorine (Roddick, 1983). Dates and errors were calculated using the procedure of

Dalrymple et al. (1981) and the constants of Steiger and Jäger (1977). Steiger and Jäger (1977) defined the decay constant for  $^{40}\text{K}$  as  $5.543 (\pm 0.010) \times 10^{-1} \text{ a}^{-1}$ ; however, more recent work by Renne et al. (2010) define the  $^{40}\text{K}$  decay constant as  $5.5545 (\pm 0.0109) \times 10^{-1} \text{ a}^{-1}$ . As such, results were checked using the decay constant of Renne et al. (2010) and all ages were found to be well within the error ranges.

Plateau and inverse isotope correlation dates were calculated using ISOPLOT v. 3.60 (Ludwig, 2008). Errors shown in the tables and on the age spectra and inverse isotope correlation diagrams represent the analytical precision at  $2\sigma$ , assuming that the errors in the ages of the flux monitors are zero. This is suitable for comparing within-spectrum variation and determining which steps form a plateau (e.g., McDougall and Harrison, 1988, p. 89). A conservative estimate of this error in the J-value is 0.5% and can be added for inter-sample comparison. The dates and J-values for the intralaboratory standard (MAC-83 biotite at 24.36 Ma; Sandeman et al., 1999) are referenced to TCR sanidine at 28.34 Ma and FCT sanidine at 28.02 Ma (Renne et al., 1998).

#### **A.7.3.2 U-Pb Analysis – Scientific Basis**

Of the four isotopes of lead (Pb) only  $^{204}\text{Pb}$  is non-radiogenic. The remaining three isotopes are produced by the complex chain decay of uranium (U) and thorium (Th).  $^{238}\text{U}$  decays to  $^{206}\text{Pb}$  with a half-life comparable to the age of the earth;  $^{235}\text{U}$  decays to  $^{207}\text{Pb}$ ; and  $^{232}\text{Th}$  decays to  $^{208}\text{Pb}$  with a half-life comparable to the age of the universe (Jaffey et

al., 1971). As with all radiometric dating methods, the U-Pb method attempts to analyze the ratio of parent to daughter isotopes to gain a closure age for a mineral past a given temperature. For the U-Pb method corrections can be made for the amount of initial or 'common'  $^{204}\text{Pb}$  in the sample by measuring the amount of  $^{204}\text{Pb}$ , then using the  $^{206}\text{Pb}/^{204}\text{Pb}$  and  $^{207}\text{Pb}/^{204}\text{Pb}$  ratios of the whole-rock to estimate the initial amounts of  $^{206}\text{Pb}$  and  $^{207}\text{Pb}$  incorporated into the sample (Parrish, 2015). These figures are then subtracted from the present-day amounts to yield the radiogenic fractions.

The decay of the naturally occurring isotopes of U produces two independent geochronometers. These are the decay of  $^{238}\text{U}$  to  $^{206}\text{Pb}$ , and the decay of  $^{235}\text{U}$  to  $^{207}\text{Pb}$  which can be used to calculate compatible sets of  $^{206}\text{Pb}/^{238}\text{U}$  and  $^{207}\text{Pb}/^{235}\text{U}$  ratios for specified values of time (Faure and Mensing, 2005). These data can be plotted on a concordia diagram to determine the ages of crystallization and any subsequent overprinting events (e.g. lead loss due to metamorphism). A concordia diagram is a plot of  $^{206}\text{Pb}/^{238}\text{U}$  vs.  $^{207}\text{Pb}/^{235}\text{U}$ , whereby the concordia curve is the locus of age equivalence for  $^{238}\text{U}$  and  $^{235}\text{U}$  decay in a closed system.

A critical assumption within the U-Pb dating method is that the sample has remained closed to U and Pb during the lifetime of the system being dated. However, mobility of Pb and especially U under low-grade metamorphic conditions and associated hydrothermal alteration means that in silicate rocks, the U-Pb system rarely remains closed (Rasbury and Cole, 2009; Bergen and Fayek, 2012; Seydoux-Guillaume et al., 2015). This is a great limitation for the method, however, the two separate decay schemes



with common parent and daughter nuclides mean that even disturbed systems can yield useful age information.

U-Pb dating can be applied to a number of minerals, however historically the most success has been achieved by using zircon ( $\text{ZrSiO}_4$ ). Zircon's crystal structure favours the incorporation of U and Th and virtually excludes Pb from the structure during formation (Speer, 1980; Parrish and Noble, 2003). Zircon is a refractory mineral and as such it is very robust and difficult to destroy in nature, where it can survive several cycles of sedimentation, metamorphism, and melting, and is difficult to dissolve in a laboratory (Parrish and Noble, 2003). Because zircon is difficult to fully recycle by dissolution in magmatic or metamorphic systems, it will commonly preserve evidence of older tectonothermal events that lead to the formation of complex, composite grains with multiple age components. Despite its robust nature, zircon can lose Pb at relatively low temperatures (Hay and Dempster, 2009); however this is a non-diffusive process related to severe radiation damage, and as such individual crystals and domains within a single crystal can be physiochemically distinct (Cherniak and Watson, 2001).

Zircon is present in most intermediate to acidic rocks and can occur in rocks of gabbroic composition. In addition, during metamorphism, if  $\text{SiO}_2$  activity is sufficiently high (as is common) zircon can form (Parrish and Noble, 2003). Also, the incorporation of older, xenocrystic zircon into a younger magma will result in the occurrence of inherited zircon. This is manifest as either single xenocrystic grains or magmatic grains containing a xenocrystic core and is moderately common in crustally derived granitic or volcanic

felsic rocks (Parrish and Noble, 2003). Inherited zircons will commonly dissolve in per-alkaline magmas, with a high Zr saturation level, but may survive in peraluminous melts (Watson and Harrison, 1983). Knowledge of the geochemistry of the protolith is, therefore, helpful in assessing likelihood of inheritance. Inherited zircons may lose some of their accumulated Pb and may be overgrown by a new zircon crystal. Despite this, one can still gain useful age information from inherited zircons, with the upper intercept (with concordia curve) of a discordant array signifying the age of inheritance, and non-zero lower intercepts giving the age of ancient disturbance (Andersen et al., 2019). Initial analysis of zircons can be achieved by the use of a binocular microscope and SEM (cathodoluminescence [CL], back scatter electron [BSE]) to determine the complexity of crystal zonation (Parrish and Noble, 2003).

Three methods are available to date minerals by the U-Pb method: these include 1) Isotope Dilution Thermal Ionization Mass Spectrometry (ID-TIMS); 2) Secondary Ion Mass Spectrometry (SIMS); and 3) Laser Ablation Inductively Coupled Plasma Mass Spectrometry (LA-ICP-MS). The Chemical Abrasion Thermal Ionization Mass Spectrometry (CA-TIMS) method is a refinement of the ID-TIMS method developed by Mundil et al. (2004) and Mattinson (2005). For this study the CA-TIMS method was used to determine the age of emplacement for one granitic intrusion.

The CA-TIMS method is capable of completely removing discordant domains in zircon that have lost Pb (e.g., zones or cracks), and then analysing the residual, undissolved zircon that has been a closed system since formation (Mattinson, 2005; Parrish, 2015).

The CA-TIMS method involves a high temperature treatment (in the range of 800° to 1100° C for up to 60 hours) to anneal the zircon lattice from natural alpha recoil damage (Mattinson, 2005 and R. Friedman, personal communication, May 25, 2010).

Subsequently the annealed zircons undergo a series of partial dissolution steps to remove zircon zones with high to progressively lower U and Th concentrations (Mattinson, 2005). Assuming that the zircons lack inheritance, precisions of better than 0.1% can be achieved, and in theory it is possible to measure the age of zircons to better than  $\pm 1$  to 2 Ma throughout geological time (Parrish and Noble, 2003; Mattinson, 2005).

#### ***U-Pb by CA-TIMS Analytical Methodology Used in Preparation of this Thesis***

Details of the procedure used for the U-Pb CA-TIMS analysis were provided by R. Friedman (personal communication, May 25, 2010) and are paraphrased below. The technique used has been modified from CA-TIMS procedures outlined in Mundil et al. (2004), Mattinson (2005), and Scoates and Friedman (2008).

After mineral separation, the clearest, crack- and inclusion-free zircon grains are selected, photographed, and then annealed in quartz glass crucibles at 900°C for 60 hours.

Annealed grains are leached in ultrapure HF (up to 50% strength, 500 mL) and HNO<sub>3</sub> (up to 14 N, 50 mL) at a maximum of 200°C for 8-16 hours (typically 175°C for 12 hours).

Zircons are rinsed with >18 M $\Omega$ .cm water and sub-boiled acetone. Masses are estimated from the dimensions (volumes) of grains. Single grains are transferred into clean

microcapsules and liners, and spiked with a  $^{233-235}\text{U}$ - $^{205}\text{Pb}$  tracer. HF and nitric acids in a 10:1 ratio, respectively, are added to liners and then placed in Parr<sup>TM</sup> high pressure device. Dissolution is achieved at 240°C for 40 hours. The resulting solutions are dried on a hotplate at 130°C, 6N HCl is added to microcapsules and fluorides are dissolved in high pressure Parr<sup>TM</sup> devices for 12 hours at 210°C. Samples are loaded onto degassed, zone-refined Re filaments in 2 mL of silicic acid emitter (Gerstenberger and Haase, 1997; R. Friedman, personal communication, May 25, 2010).

Isotopic ratios are measured using a modified single collector VG-54R or 354S (with Sector 54 electronics) thermal ionization mass spectrometer equipped with analogue Daly photomultipliers. Measurements are done in peak-switching mode on the Daly detector. Analytical blanks are 0.2 pg for U and Pb for 1 pg. U fractionation was determined directly on individual runs using the  $^{233-235}\text{U}$  tracer, and Pb isotopic ratios were corrected for fractionation of 0.23%/amu, based on replicate analyses of the NBS-982 Pb reference material and the values recommended by Thirlwall (2000). Data reduction employed the excel based program of Schmitz and Schoene (2007). Standard concordia diagrams were constructed and regression intercepts, weighted averages calculated with Isoplot (Ludwig, 2003). Unless otherwise noted, all errors are quoted at the 2 sigma or 95% level of confidence (R. Friedman, personal communication, May 25, 2010).

## Bibliography

- Andersen, T., Elburg, M. A., and Magwaza, B. N., 2019, Sources of bias in detrital zircon geochronology: Discordance, concealed lead loss and common lead correction: *Earth-Science Reviews*, v. 197, p. 1-15.
- Applied Chemical and Morphological Analysis Laboratory (ACMAL), 2014, JEOL JSM-6400 SEM: Michigan Technological University, [http://mcff.mtu.edu/acmal/electronmicroscopy/SEM\\_Form\\_Function.htm](http://mcff.mtu.edu/acmal/electronmicroscopy/SEM_Form_Function.htm), accessed 25/08/20.
- Bergen, L., and Fayek, M., 2012, Petrography and geochronology of the Pele Mountain quartz-pebble conglomerate uranium deposit, Elliot Lake District, Canada: *American Mineralogist*, v. 97, p. 1274-1283.
- Bowen, R., 2011, Radioactive Dating Methods, *in* Vértes, A., Nagy, S., Klencsár, Z., Lovas, R. G., and Rösch, F., eds., *Handbook of Nuclear Chemistry*: Boston, MA, Springer US, p. 761-816.
- Carr, J., Beatson, R., Cherrie, J., Mitchell, T., Fright, W., McCallum, B., and Evans, T., 2001, Reconstruction and Representation of 3D Objects With Radial Basis Functions: *ACM SIGGRAPH*, p. 67-76.
- Cherniak, D. J., and Watson, E. B., 2001, Pb diffusion in zircon: *Chemical Geology*, v. 172, p. 5-24.
- Dalrymple, G. B., Alexander, J., E.C., Lanphere, M. A., and Kraker, G. P., 1981, Irradiation of samples for  $^{40}\text{Ar}/^{39}\text{Ar}$  dating using the Geological Survey TRIGA Reactor: U.S. Geological Survey, Professional Paper 1176, 55 p.
- Dutrow, B. L., and Clark, C. M., 2020, X-ray powder diffraction (XRD): Science Education Resource Center at Carleton College, [https://serc.carleton.edu/research\\_education/geochemsheets/techniques/XRD.html](https://serc.carleton.edu/research_education/geochemsheets/techniques/XRD.html) accessed 24/08/20.
- Eby, G. N., 2013, Instrumental neutron activation analysis (INAA) and forensic applications: Geological Society, London, Special Publications, v. 384, p. 121-131.
- Faure, G., and Mensing, T. M., 2005, *Isotopes principles and applications*: John Wiley & Sons Inc., 897 p.
- Gerstenberger, H., and Haase, G., 1997, A highly effective emitter substance for mass spectrometric Pb isotope ratio determinations: *Chemical Geology*, v. 136, p. 309–312.
- Hay, D. C., and Dempster, T. J., 2009, Zircon behaviour during low-temperature metamorphism: *Journal of Petrology*, v. 50, p. 571-589.
- Henry, D., Eby, N., Goodge, J., and Mogk, D., 2016, X-ray reflection in accordance with Bragg's Law: Science Education Resource Center at Carleton College,

[https://serc.carleton.edu/research\\_education/geochemsheets/BraggsLaw.html](https://serc.carleton.edu/research_education/geochemsheets/BraggsLaw.html),  
accessed 25/08/20.

- Hill, E. J., Oliver, N. H. S., Cleverley, J., and Nugus, M., 2014, Modelling ore bodies of high-nugget gold using conditional probability: *Mathematics of Planet Earth*, p. 5-8.
- Hoffman, E. L., 1992, Instrumental neutron activation in geoanalysis: *Journal of Geochemical Exploration*, v. 44, p. 297-319.
- Jaffey, A. H., Flynn, K. F., Glendenin, L. E., Bentley, W. C., and Essling, A. M., 1971, Precision Measurement of Half-Lives and Specific Activities of  $^{235}\text{U}$  and  $^{238}\text{U}$ : *Physical Review C*, v. 4, p. 1889-1906.
- Jobin, D. M., Véronneau, M., and Miles, W., 2017, Gravity anomaly map, Canada / Carte des anomalies gravimétriques, Canada, in Geological Survey of Canada, Open File 8081: Natural Resources Canada, p. 1 sheet.
- Joynt, P., 2013, Leapfrog's structural trend: Inside Seequent, 2016.
- Kohli, R., and Mittal, K. L., 2019, Methods for Assessing Surface Cleanliness, *in* Kohli, R., and Mittal, K. L., eds., *Developments in Surface Contamination and Cleaning*, Volume 12: Elsevier, p. 23-105.
- Lavina, B., Dera, P., and Downs, R. T., 2014, Modern X-ray Diffraction Methods in Mineralogy and Geosciences: *Reviews in Mineralogy and Geochemistry*, v. 78, p. 1-31.
- Ludwig, K. R., 2003, User's Manual for Isoplot 3.00: A Geochronological Toolkit for Microsoft Excel, University of California at Berkeley, 74 p.
- Ludwig, K. R., 2008, User's Manual for ISOPLOT 3.60 - A Geochronological Toolkit for Microsoft Excel, Berkeley Geochronological Centre Special Publication Number 4, 54 p.
- Marshall, B. D., 1998, Potassium-calcium decay system: *Geochemistry*, Springer Netherlands, p. 525-526.
- Mattinson, J. M., 2005, Zircon U-Pb chemical abrasion ("CA-TIMS") method: Combined annealing and multi-step partial dissolution analysis for improved precision and accuracy of zircon ages: *Chemical Geology*, v. 220, p. 47-66.
- McDougall, I., and Harrison, T. M., 1988, *Geochronology and Thermochronology by the  $^{40}\text{Ar}/^{39}\text{Ar}$  Method*, 1st Edition, Oxford University Press, 212 p.
- McDougall, I., and Harrison, T. M., 1999, *Geochronology and Thermochronology by the  $^{40}\text{Ar}/^{39}\text{Ar}$  Method*, 2nd Edition, Oxford University Press, 288 p.
- McLennan, T., 2013, Interpolant function in Leapfrog Geo,  
<http://blog.leapfrog3d.com/2013/07/26/interpolant-functions-in-leapfrog-geo/#more-700>, accessed 29/11/16
- McPhar Geosurveys Ltd (McPhar), 2006, Final report on a helicopter-borne geophysical survey, Keno Hills, Yukon: unpublished report, Newmarket, Ontario, 36 p.

- Megrue, G. H., 1973, Spatial distribution of  $^{40}\text{Ar}/^{39}\text{Ar}$  ages in Lunar Breccia 14301: *Journal of Geophysical Research*, v. 78, p. 3216-3221.
- Merrihue, C., 1965, Trace-element determinations and potassium-argon dating by mass spectroscopy of neutron-irradiated samples: *Transactions of the American Geophysical Union*, v. 46, p. 125.
- Miles, W., and Oneschuk, D., 2016, Magnetic anomaly map, Canada / Carte des anomalies magnétiques, Canada: Geological Survey of Canada, Open File 7799, Natural Resources Canada, 1 sheet.
- Mundil, R., Ludwig, K. R., Metcalfe, I., and Renne, P. R., 2004, Age and timing of the Permian mass extinctions: U/Pb dating of closed-system zircons: *Science*, v. 305, p. 1760.
- O'Connor, L., Lippoth, R., and Stammers, M., 2007, 2006 geophysical, aerial photography and orthophoto assessment report on the Keno Hill property: unpublished report, Alexco Resource Corp. and United Keno Hill Mines Limited in Receivership,
- Oneschuk, D., Miles, W., Saltus, R., and Hayward, N., 2019, Alaska and Yukon magnetic compilation, residual total magnetic field: Geological Survey of Canada, Open File 7862, Natural Resources Canada, p. 1 sheet.
- Parrish, R., 2015, Uranium–Lead Dating, *in* Rink, W. J., Thompson, J. F. H., Heaman, L. M., Jull, A. J. T., and Paces, J. B., eds., *Encyclopedia of scientific dating methods*. *Encyclopedia of earth sciences*: Springer Reference, p. 848-858.
- Parrish, R. R., and Noble, S. R., 2003, Zircon U-Th-Pb geochronology by isotope dilution — Thermal Ionization Mass Spectrometry (ID-TIMS): *Reviews in Mineralogy and Geochemistry*, v. 53, p. 183-213.
- Potts, P. J., and Webb, P. C., 1992, X-ray fluorescence spectrometry: *Journal of Geochemical Exploration*, v. 44, p. 251-296.
- Rasbury, E. T., and Cole, J. M., 2009, Directly dating geologic events: U-Pb dating of carbonates: *Reviews of Geophysics*, v. 47, p. 1-27.
- Renne, P. R., Mundil, R., Balco, G., Min, K., and Ludwig, K. R., 2010, Joint determination of  $^{40}\text{K}$  decay constants and  $^{40}\text{Ar}^*/^{40}\text{K}$  for the Fish Canyon sanidine standard, and improved accuracy for  $^{40}\text{Ar}/^{39}\text{Ar}$  geochronology: *Geochimica et Cosmochimica Acta*, v. 74, p. 5349-5367.
- Renne, P. R., Swisher, C. C., Deino, A. L., Karner, D. B., Owens, T. L., and DePaolo, D. J., 1998, Intercalibration of standards, absolute ages and uncertainties in  $^{40}\text{Ar}/^{39}\text{Ar}$  dating: *Chemical Geology*, v. 145, p. 117-152.
- Roddick, J. C., 1983, High precision intercalibration of  $^{40}\text{Ar}$ - $^{39}\text{Ar}$  standards: *Geochimica et Cosmochimica Acta*, v. 47, p. 887-898.
- Sandeman, H. A., Archibald, D. A., Grant, J. W., Villeneuve, M. E., and Ford, F. D., 1999, Characterization of the chemical composition and  $^{40}\text{Ar}$ - $^{39}\text{Ar}$  systematics of

- intralaboratory standard MAC-83 biotite, radiogenic age and isotopic studies: Report 12; Geological Survey of Canada, Current Research no. 1999-F, p. 13-26.
- Schmitz, M. D., and Schoene, B., 2007, Derivation of isotope ratios, errors, and error correlations for U-Pb geochronology using  $^{205}\text{Pb}$ - $^{235}\text{U}$ -( $^{233}\text{U}$ )-spiked isotope dilution thermal ionization mass spectrometric data: *Geochemistry, Geophysics, Geosystems*, v. 8, p. 1-20.
- Scoates, J., and Friedman, R., 2008, Precise age of the platiniferous Merensky reef, Bushveld Complex, South Africa, by the U-Pb zircon chemical abrasion ID-TIMS technique: *Economic Geology*, v. 103, p. 465-471.
- Seydoux-Guillaume, A.-M., Bingen, B., Paquette, J.-L., and Bosse, V., 2015, Nanoscale evidence for uranium mobility in zircon and the discordance of U-Pb chronometers: *Earth and Planetary Science Letters*, v. 409, p. 43-48.
- Speer, J. A., 1980, Zircon: Reviews in Mineralogy and Geochemistry, v. 5, p. 67-112.
- Spragg, K., 2013a, Interpolation and anisotropy, Inside Seequent, 2016.
- Spragg, K., 2013b, Leapfrog interpolation basics, Inside Seequent, 2016.
- Steiger, R. H., and Jäger, E., 1977, Subcommittee on geochronology: Convention on the use of decay constants in geo- and cosmochemistry: *Earth and Planetary Science Letters*, v. 36, p. 359-362.
- Thirlwall, M. F., 2000, Inter-laboratory and other errors in Pb isotope analyses investigated using a  $^{207}\text{Pb}$ - $^{204}\text{Pb}$  double spike: *Chemical Geology*, v. 163, p. 299-322.
- Wänke, H., and König, H., 1959, Eine neue methode zur kalium-argon-altersbestimmung und ihre anwendung auf steinmeteorite: *zeitschrift für naturforschung A*, v. 14, p. 860.
- Watson, E. B., and Harrison, T. M., 1983, Zircon saturation revisited: temperature and composition effects in a variety of crustal magma types: *Earth and Planetary Science Letters*, v. 64, p. 295-304.
- Wirth, K., and Barth, A., 2020, X-ray fluorescence (XRF): Science Education Resource Center at Carleton College, [https://serc.carleton.edu/research\\_education/geochemsheets/techniques/XRF.html](https://serc.carleton.edu/research_education/geochemsheets/techniques/XRF.html), accessed 24/08/20
- York, D., Hall, C. M., Yanase, Y., Hanes, J. A., and Kenyon, W. J., 1981,  $^{40}\text{Ar}/^{39}\text{Ar}$  dating of terrestrial minerals with a continuous laser: *Geophysical Research Letters*, v. 8, p. 1136-1138.